BOND-SLIP RESPONSE OF STEEL FIBERS AFTER EXPOSURE TO ELEVATED TEMPERATURES: EXPERIMENTAL PROGRAM AND DESIGN-ORIENTED CONSTITUTIVE EQUATION

Ramoel Serafini[1,2*], Ronney Rodrigues Agra[1,2], Luís A. G. Bitencourt Jr.[3], Albert de la Fuente[4], Antonio D. de Figueiredo[1]

[1]Department of Civil Construction Engineering, Polytechnic School at the University of São Paulo | Avenida Professor Almeida Prado, Travessa do Biênio, 83, 05424-970, São Paulo, Brazil.

[2] Institute of Technological Research | Avenida Professor Almeida Prado, 532, 05508-901, São Paulo, Brazil

[3] Department of Structural and Geotechnical Engineering, Polytechnic School at the University of São Paulo | Avenida Professor Almeida Prado, Travessa do Biênio, 83, 05424-970, São Paulo, Brazil.

[4] Department of Construction Engineering, Polytechnic University of Catalonia | Jordi Girona, 1-3, 08034, Barcelona, Spain

*corresponding author: rserafini@usp.br

Keywords: pullout; bond-slip response; hooked-end steel fibers; elevated temperatures; numerical simulation

ABSTRACT

This study aimed to evaluate the effect of elevated temperatures on the bond-slip behavior of hooked-end steel fibers. A total of 180 pullout specimens were tested in post-cooling conditions using a double-sided pullout test with multiple embedded fibers for target temperatures between 25 and 750 °C. Results proved that the bond strength significantly increases for temperatures up to 450 °C, and drastically decreases for temperatures of 600 and 750 °C. The contribution of hooks reduced with temperature and is negligible for temperatures higher than 600 °C, while the fiber-matrix frictional interaction seems to improve for all temperatures evaluated. A

temperature-sensitive constitutive equation that allows simulating the bond-slip behavior of hooked-end steel fibers is proposed and its suitability confirmed through a numerical model.

1 Introduction

The fundamental principle of steel fiber reinforced concrete (SFRC) is based on the interaction between fibers and the cementitious matrix to provide plain concrete a pseudo-ductile behavior and enhance post-crack mechanical properties. The steel fibers bridge the cracks through the matrix and enhance the post-crack tensile strength of the composite, which is a key feature for structural applications [1,2]. Three main components that must be characterized to analyze these composites after temperature exposure are the cementitious matrix, the fibers, and the fiber-matrix interface. In this regard, the bond-slip response between the fiber and the cementitious matrix is a key parameter to model the SFRC mechanical behavior [3] and is known to strongly influence the post-crack behavior of the composite [4,5]. The bond-slip response of hooked-end steel fibers in the cementitious matrix can be parameterized by pullout test results and can be divided into five main stages [6], which are schematically shown in Figure 1.

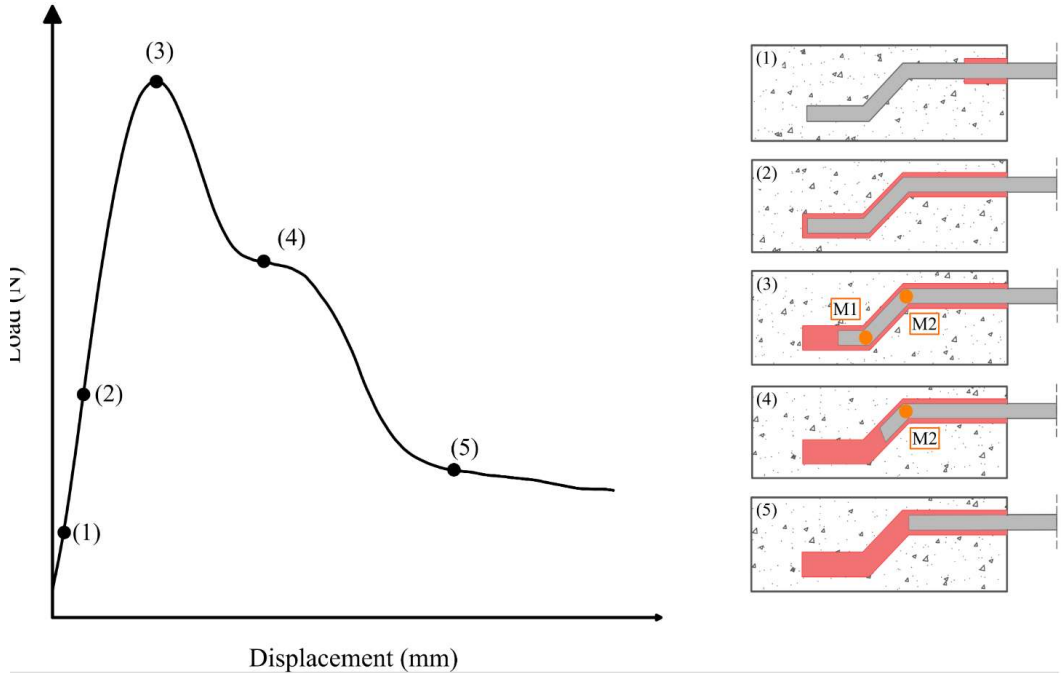

Figure 1 – Schematic diagram of the pullout mechanism for hooked-end steel fibers

Stage 1 and 2 are defined as the partial and full debonding between fiber and matrix, respectively. Once the full debonding takes place, the dynamic frictional interaction between fiber and matrix begins. At this stage, the fibers must undergo a considerable plastic deformation due to the straightening of the hooks before the dynamic frictional interaction occurs [6], which defines Stages 3 and 4. The mechanical interlocking caused by the plastic deformation of the hooks at M1 and M2 increases the maximum pullout load value at Stage 3.

As soon as the tip of the fiber goes beyond M1, the pullout load substantially decreases and the mechanical interlocking is caused only by the plastic deformation of the hook at M2. It is important to remind that the matrix cracks as the pullout occurs [5] and that the energy required to yield the hooks is intrinsically bound to the bending stiffness and the hook geometry of the steel fiber, as well as the interfacial bond properties [7,8]. After the hook is completely straightened, the dynamic frictional interaction between fiber and matrix takes place in Stage 5. This last phase results in a rapid drop in the pullout load values and prevails until the whole fiber is removed from the matrix pathway [6].

Pullout tests are conducted in a wide variety of setups in the literature. The difference between methodologies adopted is usually related to the number of fibers embedded (single or multiple fibers) and the method of applying the tensile force (single- or double-sided). The pullout tests are commonly performed employing single-sided tests on a single fiber, owing to the simplicity of the methodology during the preparation of specimens and during the test [6]. However, a major drawback of this methodology is that the test setup needs to be capable of precision measurements due to the intrinsically low pullout forces. More than that, difficulties encountered in single-sided tests are mainly associated with the interaction between the grip and the fiber. Also, high variability is common in single-sided tests on a single fiber, which requires a considerable number of specimens to guarantee the reliability of the results [9].

The drawbacks of using single-sided tests with a single fiber are further aggravated for pullout specimens that are exposed to elevated temperatures. This occurs because the pullout forces are expected to reduce and the steel fiber mechanical properties to be negatively affected after high-temperature exposure. Several studies have investigated the bond-slip properties of hooked-end steel fibers at room temperature conditions in the last decades [9–12]. However, the studies regarding the bond-slip behavior of steel fibers after elevated temperatures are very scarce in the literature. In this sense, there is a need for identifying constitutive equations and analytical formulations to the designers' community so that the effect of fire on SFRC structures can be properly assessed.

Results obtained by recent studies show that the pullout load values were comparable up to ~400 °C and significantly reduced for higher temperatures [13–16]. However, the non-significant effect of temperature up to 400 °C may be a side effect of the intrinsic dispersion of single-sided tests with a single fiber, since the standard deviation values were omitted. Moreover, numerical models focusing on the explicit and discrete representation of the steel fibers in SFRC have been developed recently and require an accurate description of the steel fiber bond-slip behavior as input [17,18]. So far, the results published in the literature have not provided a microstructural based explanation for the changes in the bond-slip behavior or proposed a constitutive equation for design purposes, which denotes that the topic still needs to be deeply investigated.

The present study aims to evaluate the bond-slip behavior of hooked-end steel fibers after exposure to elevated temperatures employing a double-sided pullout test using multiple fibers. This test methodology aims at increasing the stability of the test and avoiding the drawbacks associated with single-sided and single fiber pullout tests. The interfacial transition zone of the steel fibers was characterized to assess the effect of temperature on the vicinity of the fiber and relate the microstructural results with the mechanical behavior. Additionally, an analytical

model was proposed and the pullout tests were validated through numerical simulations using a discrete and explicit representation of steel fibers inside the pullout specimens.

2 Materials and methods

Figure 2 shows a schematic drawing of the experimental program conducted in this study. The investigation herein conducted took place within the framework of a Ph.D. research project regarding the study of the effect of temperature on the properties of fiber-reinforced composites. In this sense, all the characterizations were conducted using a mortar that followed the SFRC mix design based on the work of Serafini et al. [19] and a detailed description and characterization of the materials employed can be found in the referenced study. Even with those considerations, a brief description is presented in this section.

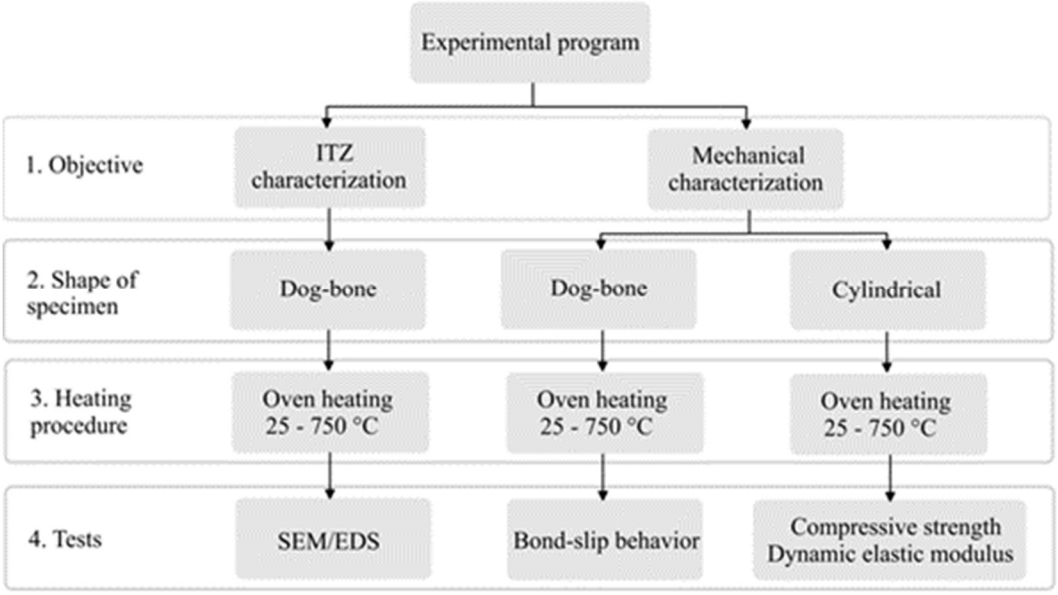

Figure 2 – Scheme adopted for the experimental program of this study

The bond-slip response of the hooked-end steel fibers was evaluated after exposure to high temperatures. Based on the experimental results, an analytical equation that computes the effect of temperature on the bond-slip behavior of steel fibers is proposed. This equation is used as input for a refined numerical model that is capable of representing the steel fibers discretely and explicitly inside the plain concrete [18]. As supplementary investigations, the characterization

of the interfacial transition zone (ITZ) is performed and aims to verify the effect of temperature on the vicinity of the fiber, which can be correlated with the bond-slip response. Additionally, the effect of temperature on the compressive strength and dynamic elastic modulus of the mortar were evaluated and serve as input for the numerical simulation conducted in this study.

2.1 Materials

The cementitious materials used in this study were a Type I Portland cement (CEM I 52.5R) and silica fume type Elkem 920-U. The particle packing was increased by using river and artificial sand as fine aggregates and two coarse granite aggregates. A polycarboxylate-based superplasticizer, GCP ADVA Cast 525, was used to provide consistency to the mix. A cold-drawn, hooked-end steel fiber, Dramix 3D 80/60-BG, was employed. This steel fiber was chosen since it is commonly used in structural applications. The explosive spalling phenomenon was mitigated by the addition of Neomatex FireX polypropylene microfibers. Table 1 shows fiber manufacturer data for both fiber types.

Table 1 – Fiber manufacturer data for both fiber types

Characteristics	Hooked-end steel fiber	Micro-synthetic fiber
Length (mm)	60	12
Diameter (mm)	0.75	0.03
Aspect ratio (l/d)	80	400
Specific weight (kg/m^3)	7850	910
Specific surface area (m^2/kg)	3.45	147
Melting point (°C)	~1370	165
Tensile strength (MPa)	1225	Not provided
Young modulus (GPa)	210	Not provided

2.2 Composition and preparation of mortar

The composition of the mortar was based on the mix design of the precast segments used in tunnel linings of Subway Line 6 of São Paulo [19], which is described in Table 2. Silica fume

was used as supplementary cementitious material at a content of 5.5% of the cement mass, and the w/cm ratio was kept constant at 0.39. All aggregates were oven-dried at 100 °C for 14 h before mortar production. Synthetic micro-fibers were added in a content of 0.15% of the total volume, or 1.4 kg/m^3, according to project specifications, to avoid damage of the mortar due to explosive spalling.

Table 2 – Dosage of materials to produce 1 m^3 of mortar

Materials	Dosage (kg/m³)
Portland cement	700
Silica fume	39
Water	289
Siliceous river sand	705
Artificial granite sand	471
Superplasticizer	5.25
Synthetic micro-fiber	1.4

The mortar mixing was conducted by using a planetary Hobart N50 mixer with a total capacity of 5 L in a room at (25 ± 1) °C. The following procedure was adopted: microfibers were added to the bowl and dispersed with water for 90 seconds. This period was divided into 30-30-30 seconds in, respectively, low-high-low speed. Then, the fine aggregates, cement, and silica fume were added during 60 seconds with the equipment turned off and 30 seconds were given for particle wetting. At last, water and dry powder were mixed for 90 seconds, following the same 30-30-30 seconds in low-high-low speed. The aforementioned mixing procedure was adopted since it results in better homogenization of materials and microfibers according to Dantas et al. [20]. A total of 30 cylindrical specimens with a diameter of 50 mm and a height of 100 mm were produced to assess the compressive strength and the dynamic elastic modulus of the material.

Pullout specimens in the shape of dog-bones were produced to assess the bond-slip behavior of the hooked-end steel fibers. Figure 3 shows the dimensions of the pullout specimens produced. The pullout specimens were manufactured using four steel fibers instead of the usual single fiber, which had as objective to increase the stability of the test. This was adopted by the authors as a countermeasure to the intrinsic low pullout load values of single-fiber pullout tests, which are made even more severe by the exposure to elevated temperatures [13,14,16]. A total of 180 pullout specimens were produced and tested in this study.

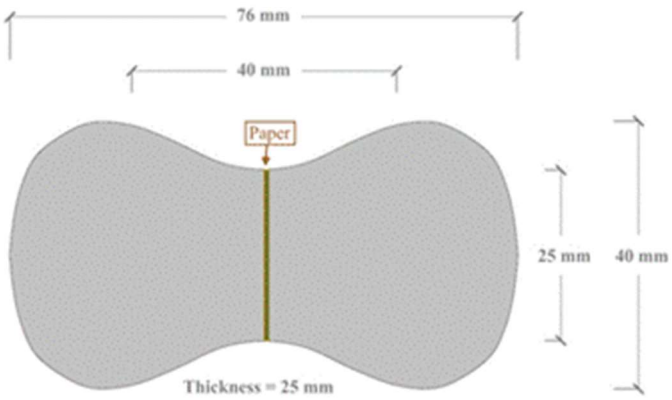

Figure 3 – Dimensions of the pullout specimen produced

Figure 4 illustrates the molding procedure, the fixation frame, and the pullout specimen produced. The four steel fibers were positioned in the middle of the molds with a measured embedded length of 30 mm at each side and separated by a distance of 10 mm between the fibers. Since the embedded lengths are the same on both sides, the pullout may occur from either side without any detrimental effect on the results. In cases where different embedded lengths are adopted, the methodology must ensure that the four fibers are pulled out from the same side of the specimen to ensure the reliability of the results.

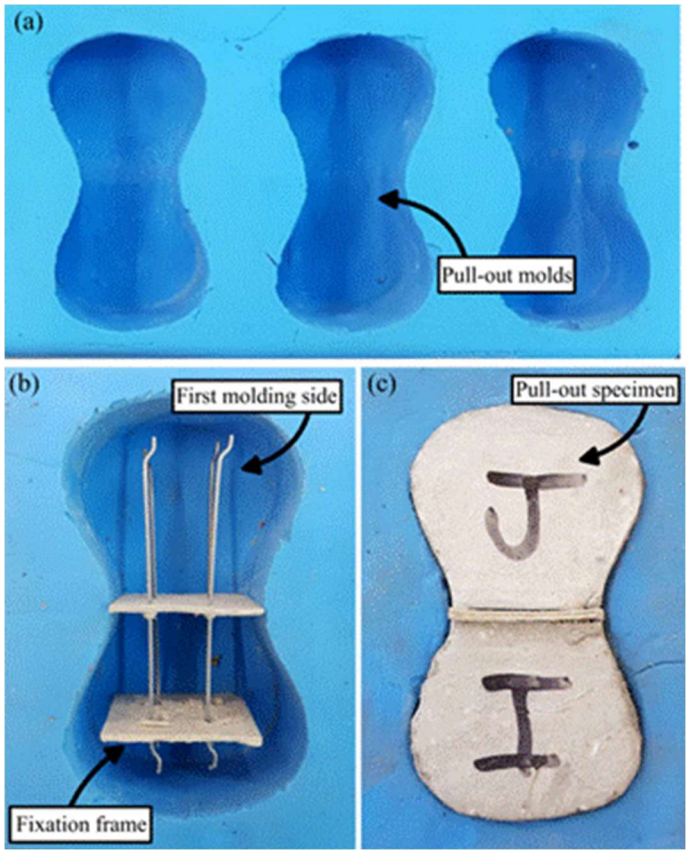

Figure 4 – Molding procedure: (a) the pullout molds (b) fixation frame (c) pullout specimen

Two papers of 250 g/m^2 were used to fix the steel fibers inside the mold. This procedure had the objective of preventing the steel fibers from moving or rotating inside the pullout specimens. After that, the mortar was poured inside one half of the mold. The embedded length was double-checked on the empty side of the mold and, after 4 hours, the fixation frame was removed, and the other half of the mold was filled with mortar. After the molding procedure, the pullout molds were sealed with a protective plastic film during 12 h until the specimens could be removed from the mold. After demolding, the pullout specimens were cured in a humid chamber for 72 h and then stored at room temperature of (25 ± 1) °C until the age of 150 days to better simulate *in situ* humidity and curing conditions.

2.3 Heating procedure

The cylindrical and pullout specimens were heated using an EDG FC series electric oven, model EDG10P-S, at a heating rate of (20 ± 3) °C/min at the age of 150 days. The period at target temperature adopted was determined by numerical simulation to ensure the thermal stability of

the specimens based on the work of Carpio et al. [21]. Therefore, the pullout specimens were kept at target temperatures during 10, 8, 6, 4, and 4 h for the respective temperatures of 150, 300, 450, 600, and 750 °C. After the heat exposure was over, the chamber was kept closed and cooling until the room temperature was achieved for 24 h. The cooling rate was not controlled. After cooling, both the cylindrical and pullout specimens were taken for mechanical testing. Figure 5 shows the heating procedure adopted for the cylindrical and pullout specimens.

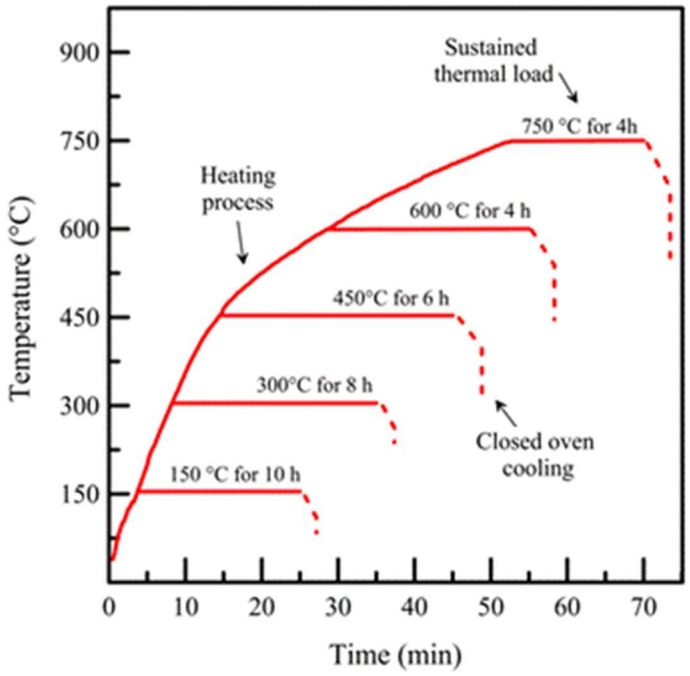

Figure 5 – Heating procedure adopted for cylindrical and pullout specimens

2.4 Test method

2.4.1 Compressive strength test

The compressive strength tests were conducted on a Shimadzu Universal Testing Machine, model UH-F1000kN, with a computer-controlled hydraulic servo system, and a maximum load capacity of 1,000 kN. The test was load-controlled at a rate of 0.5 MPa/s and piston displacement data was used to calculate the strain values during the test. A total of 30 specimens were tested, 5 for each target temperature: 25, 150, 300, 450, 600, and 750 °C.

2.4.2 Ultrasonic pulse velocity test

189 The ultrasonic (US) propagation test was conducted by using a Portable Ultrasonic Non-
190 destructive Digital Indicating Tester (PUNDIT) equipment using 200 kHz transducers and a
191 circular cross-section with a 20 mm diameter. The US propagation velocity was determined in
192 the same specimens before and after temperature exposure and used to determine the dynamic
193 elastic modulus (E_c) of the mortar before and after temperature exposure, calculated as:

$$E_c = \frac{\rho . V^2 . (1 + v) . (1 - 2v)}{1 - v} \quad \text{Eq. (1)}$$

194 where ρ is the density of the mortar (in kg/m^3); V is the propagation pulse velocity (in km/s);
195 v is the Poisson's ratio). The density of the material was recalculated for each target temperature
196 based on the mass and volume of the specimens. Although data about the effect of temperature
197 on Poisson's ratio are relatively scarce and tend to be inconsistent, the results found in the
198 literature show that this property does not change significantly for small stress values [22].
199 Therefore, the Poisson's ratio was assumed to be constant at 0.2 for all target temperatures.

200 **2.4.3 Fiber-matrix interface**

201 The effect of elevated temperatures on the fiber-matrix interface was evaluated through
202 Scanning Electron Microscopy (SEM) with Energy Dispersive Spectroscopy (EDS) for a more
203 in-depth analysis of the results. Line scanning EDS analyses were conducted to obtain the
204 surface chemical profile concerning the radial distance from the fiber, represented by the red
205 line in the example presented in Figure 6.

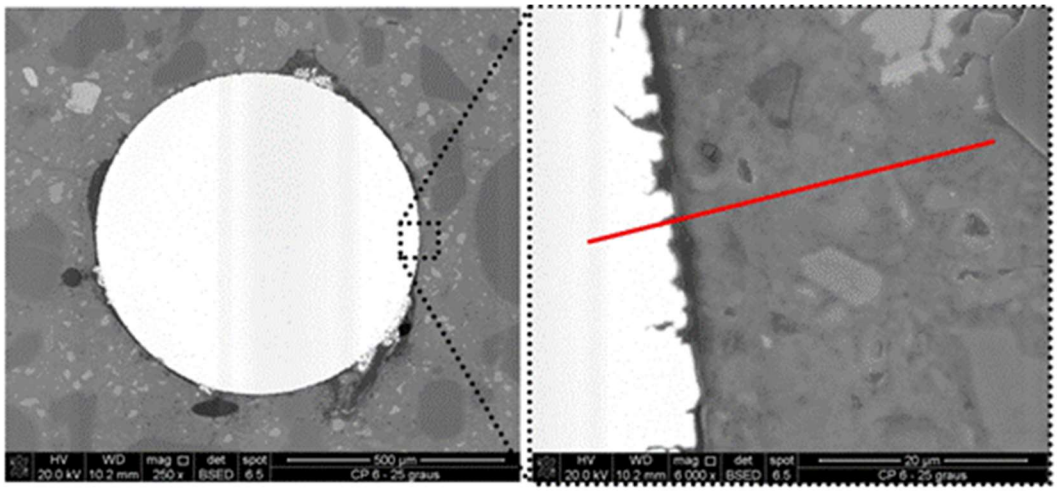

Figure 6 – EDS analysis conducted to obtain the surface chemical profile in the vicinity of the fiber

Samples were prepared by using the dog-bone shaped pullout specimens after the heat procedure and mechanical testing was conducted. The pullout specimens were sliced with a precision saw and the region around the fiber was analyzed in samples measuring 25 x 25 x 25 mm. The samples were embedded in resin and plane ground employing 150 µm grained sandpaper and fine ground employing 9 µm grained sandpaper for 10 minutes at the 1000 and 150 rpm, respectively. After grinding, the samples were dry-polished using a 2 µm diamond polishing cloth specific for metallographic purposes. Samples were then taken for SEM/EDS analysis in the Center for Metallurgical and Materials Technologies (CTMM) at the Institute for Technological Research (IPT). SEM/EDS tests were conducted using a Quanta 3D FEG instrument, equipment at the voltage of 20 kV, working distance of 10 mm, using XT microscope control FEI software to obtain backscattered electron imagery.

The calcium (Ca) and silicon (Si) contents were determined by EDS and can be used as an indirect method to assess the composition of the cementitious matrix utilizing the Si/Ca ratio [23]. Additionally, the contents of iron (Fe), oxygen (O), and carbon (C) were determined and served as a means to assess the changes in steel and the location of fracture surfaces.

2.4.4 Pullout test

Figure 7 illustrates the pullout test setup conducted in this study. The pullout tests were conducted using an electromechanical universal testing machine in an open-loop configuration,

EMIC DL 10000, with a load-cell with a maximum load capacity of 10 kN and precision of 1 N. The test was displacement-controlled at a rate of 0.5 mm/min. The load cell was placed on the top of the machine crosshead to read the fiber pullout force while the slip between the fiber and matrix was determined by piston displacement readings. The initial accommodation was minimized by slowly applying the load to the specimens until some load was recorded by the load cell before initiating the test.

Figure 7 – Pullout test setup conducted in this study

The pullout test was stopped before the complete pullout of the fiber from the specimen occurred. This was adopted because the failure criteria established into the design guidelines (i.e. maximum crack width of 2.5 mm according to the *fib* Model Code 2010 [24]) is achieved before the full embedded length (30 mm) is pulled out of the matrix. Therefore, the pullout tests of this study were conducted until a displacement of 10 mm was achieved, since any result

obtained for greater displacement values would have no useful application from the engineering standpoint. In this sense, 30 pullout tests were performed for each target temperature of 25, 150, 300, 450, 600, and 750 °C, representing a total of 180 specimens.

Furthermore, the pullout curves obtained from the pullout tests were normalized to be representative of a single fiber pullout. This was achieved by dividing the pullout curves by the amount of resisting fibers in each section of the test. This normalization was required to make a valid comparison with the literature results. Additionally, the rupture of some fibers occurred in specimens exposed to elevated temperatures, thus, this normalization was strictly necessary to guarantee the validity of the comparison.

2.4.5 Statistical analysis

The compressive strength and dynamic elastic modulus of the mortar, as well as the results of bond-slip results obtained in this study, were statistically analyzed through analysis of variances (ANOVA) and Tukey tests [25]. The relationship between the sample size and the admissible error was determined only for the variables associated with the bond-slip response of the hooked-end steel fibers since this topic is the main contribution of this study. In this sense, the relationship between the sample size and the admissible error was determined based on concepts of inferential statistics [26], as follows:

$$n = \frac{s^2 \cdot z_\gamma{}^2}{\varepsilon^2} \qquad \text{Eq. (2)}$$

where n is the required sample size; s is the standard deviation obtained by the pilot sample (in MPa); z_γ is the Student's t-distribution value; ε is the admissible error for the test. The average and standard deviation values were determined based on the experimental campaign conducted, while a t-distribution value was adopted considering a confidence interval of 95% and $(n-1)$ degrees of freedom.

3 Results and discussion

3.1 Compressive strength and elastic modulus

Figure 8 illustrates the density values and pulse velocity changes as a function of temperature. Table 3 shows the average results for the density and pulse velocity of mortar before and after temperature exposure.

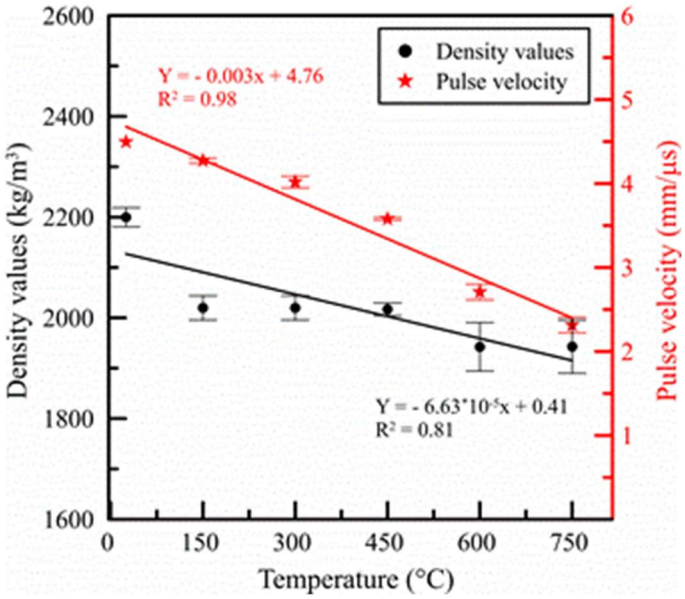

Figure 8 – Average density values and pulse velocity changes as a function of temperature

Table 3 – Average results for the density and US propagation velocity of the mortar

Temperature (°C)	Before temperature exposure		After temperature exposure	
	Density (kg/m³)	Pulse velocity (mm/µs)	Density (kg/m³)	Pulse velocity (mm/µs)
25	2200 (± 19)	4.50 (± 0.06)	Not applicable	Not applicable
150	2186 (± 23)	4.52 (± 0.04)	2020 (± 24)	4.27 (± 0.03)
300	2192 (± 16)	4.52 (± 0.06)	2020 (± 24)	4.02 (± 0.07)
450	2212 (± 9)	4.52 (± 0.11)	2017 (± 13)	3.58 (± 0.02)
600	2202 (± 25)	4.53 (± 0.08)	1942 (± 48)	2.71 (± 0.09)
750	2186 (± 23)	4.50 (± 0.11)	1943 (± 53)	2.31 (± 0.09)

The reductions in density values were of 7.6%, 7.9%, 8.8%, 11.8%, and 11.1% for the respective temperatures of 150, 300, 450, 600, and 750 °C. Reductions were also observed in terms of the

ultrasonic pulse velocity, which were 5.4%, 11.1%, 20.9%, 40.3%, and 48.5% for the same respective temperatures. As temperature increases, the release of free water and the dehydration of hydrated products of the cement paste occurs [19,27]. This dehydration is responsible for the reduction in the specific surface area of the hydrates and the coarsening of the pore structure, which increases the porosity of the cement paste [27,28], the increase in capillarity pore size, and the generation of cracks [29]. The aforementioned changes significantly contribute to the reductions in terms of density values and ultrasonic pulse velocity evidenced in this study.

Figure 9 shows the stress-strain curves and the residual values of compressive strength (f_c) and dynamic elastic modulus (E_c) as a function of temperature for the mortar used in this study. The average results can be found in Table 4. Specimens tested at room temperature presented an average compressive strength of 89.3 MPa and an average elastic modulus of 40.0 GPa.

Table 4 – Average results in terms of mechanical properties for each target temperature

Target temperature (°C)	f_c (MPa)	E_c (GPa)
25	89.3 (± 6.4)	40.0 (± 1.3)
150	85.5 (± 3.2)	34.2 (± 0.5)
300	72.3 (± 5.3)	29.4 (± 1.3)
450	57.6 (± 3.4)	23.2 (± 0.3)
600	42.3 (± 5.0)	12.8 (± 1.1)
750	26.0 (± 3.4)	9.4 (± 0.6)

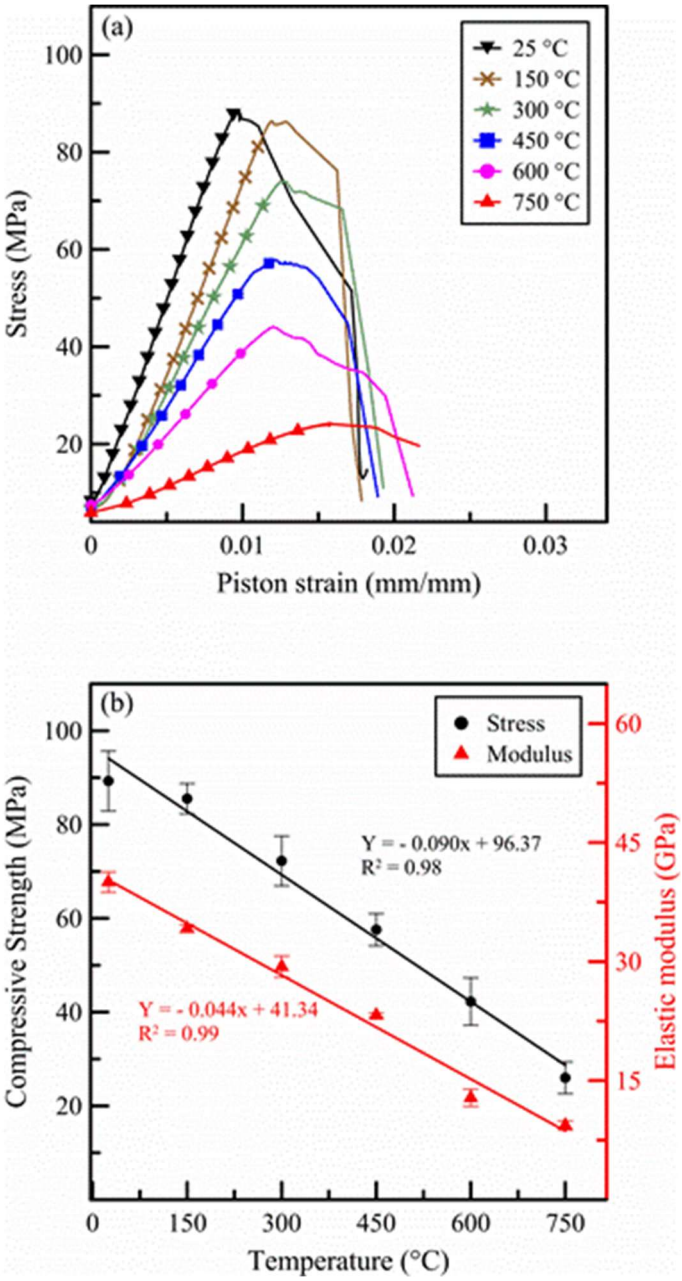

Figure 9 – (a) Stress-strain curves and (b) residual values of compressive strength and dynamic elastic modulus as a function of temperature

The residual compressive strength values after temperature exposure of 150, 300, 450, 600, and 750 °C were, respectively, 4.2%, 19.1%, 35.5%, 52.7%, and 70.9% lower than the value reached at room temperature (89.3 MPa). The changes in terms of elastic modulus may be qualitatively observed by analyzing the slope of the stress-strain curves shown in Fig. 9a. The dynamic elastic modulus results denote a reduction trend of 14.9%, 27.1%, 43.0%, 68.5%, and 76.5% for the respective target temperatures of 150, 300, 450, 600, and 750 °C when compared to room temperature (40 GPa). It is possible to observe that the properties of compressive strength and

295 elastic modulus linearly reduce with temperature increase. The elastic properties of the
296 composite are significantly affected by the changes in the cement paste pore structure caused
297 by the dehydration of hydrated products [19]. The reduction trend observed for the compressive
298 strength and elastic modulus of the mortar is in line with the results found in the literature
299 conducted in comparable conditions [30,31].

300 **3.2 Interfacial transition zone properties**

301 Figure 10 shows the fiber-matrix interface obtained by SEM analysis as a function of
302 temperature. The region analyzed with EDS is indicated by the red line. Figure 11 illustrates
303 the line scanning EDS results in the fiber-matrix interface as a function of temperature.

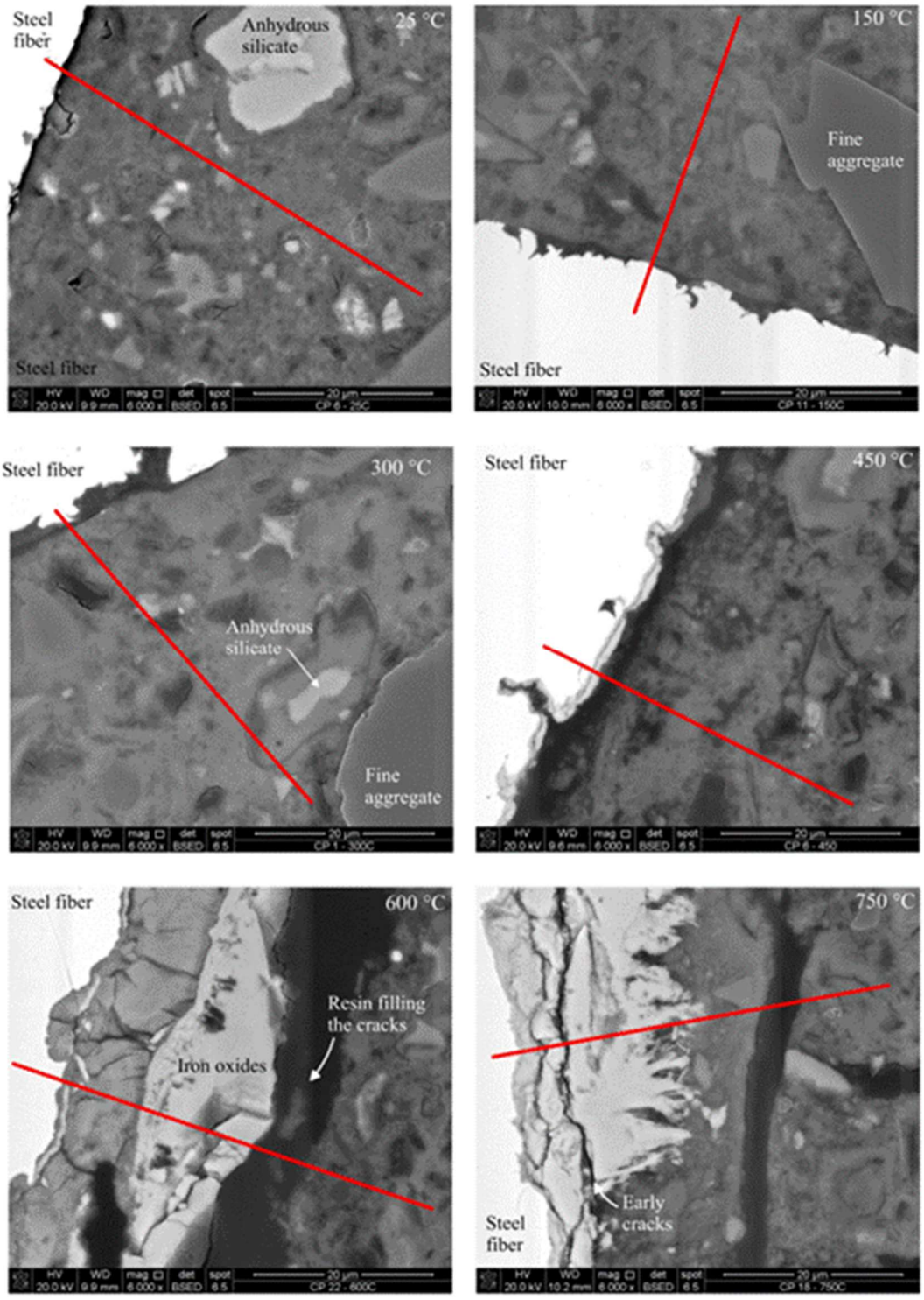

304

305 Figure 10 – Fiber-matrix interface obtained by SEM analysis as a function of temperature

306

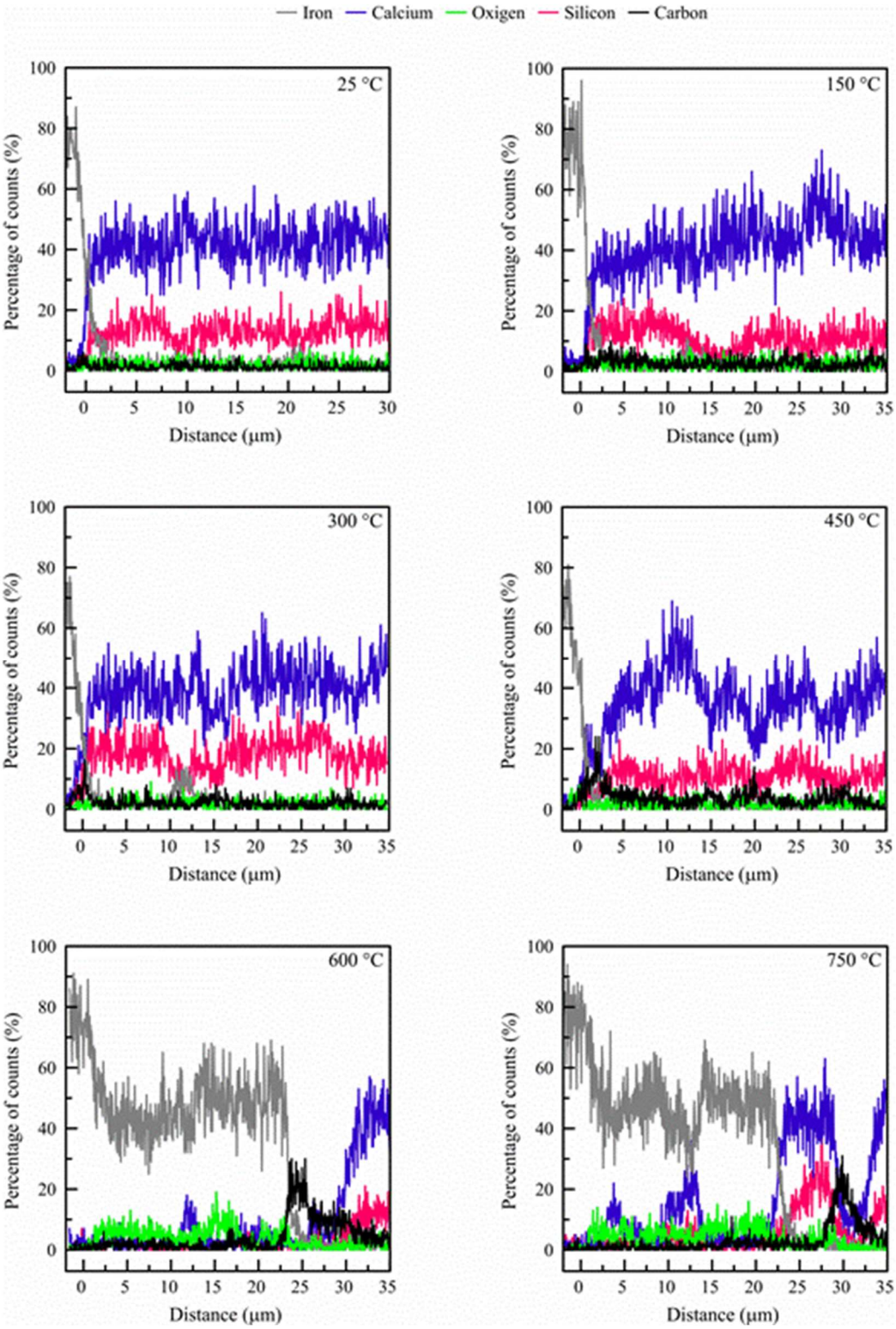

Figure 11 – Line scanning EDS results in the fiber-matrix interface as a function of maximum temperature

The qualitative evaluation of SEM images provided in Fig. 10 shows that the oxidation of the steel fibers begins at ~450 °C and increases significantly for temperatures of 600 and 750 °C. Literature results show that this oxide phase is a three-layered scaled structure composed of wüstite (FeO), hematite (Fe_2O_3), and magnetite (Fe_3O_4) and that this oxide product has higher

mass and lower density than the original steel structure, which results in the significant increase in terms of the external diameter of the steel fibers. Results in the literature point out to an increase of 3.8% in total diameter (steel + oxide) after exposure to 750 °C [32]. Also, the iron oxide may expand into the interfacial transition zone porosity for temperatures of 600 °C and above, which is denoted by the overlap of Si, Ca, Fe, and O peaks in the EDS results (see Fig. 11).

Cracks were formed in the vicinity of the fiber can be verified by analyzing the cracks filled with resin (see Fig. 10), as well as by the peak of carbon determined by EDS (see Fig. 11). This crack formation can be attributed to the detachment of fibers from the cementitious matrix and the passive thrust generated by the expansive oxidation process suffered by steel fibers. The debonding of fibers during the pullout test seems to occur in the region between the steel fiber and the interfacial transition zone for temperatures up to 450 °C. For temperatures of 600 °C and above the debonding of fibers seems to occur in the interface between the iron oxide formed and the interfacial transition zone. This rupture pattern change may result in changes in the fracture energy associated with the debonding of steel fibers and the energy dissipated during the slip portion of the test since the oxide formation increases the total diameter of the fiber [33,34].

It is worth highlighting that the cracks filled with resin are the only cracks that may be evaluated in SEM imagery since they were generated before the resin was applied. A few “early cracks” that are not filled with resin can be also noticed in Fig. 11, however, those must not be interpreted as a result of the pullout test or temperature exposure since they are likely to be generated by the vacuum applied during preparation and testing of samples, or even due to the influence of the beam of electrons during the SEM test.

Figure 12 shows the Si/Ca ratio as a function of temperature and distance from the fractured surface. For room temperature conditions, values of Si/Ca ratio lower than 0.3 represent systems with a high content of portlandite crystals and reduced amount of C-S-H, while Si/Ca ratios

greater than 0.3 indicate systems rich in C-S-H [35]. Some studies conducted also show that systems formed mainly by C-S-H show a Si/Ca ratio of 0.5 or more in the form of α-C-S-H (1 ≤ Si/Ca < 1.5), β-C-S-H (0.66 < Si/Ca <1), and γ-C-S-H (0.5 < Si/Ca < 0.66) [36]. The results obtained for specimens tested at room temperature (25 °C) present a Si/Ca ratio between 0.1 and 0.3 for the first 10 µm from the fracture surface, which denotes that portlandite tends to precipitate around the steel fiber and a low amount of C-S-H is present in this interface, which is in agreement with classical literature [5].

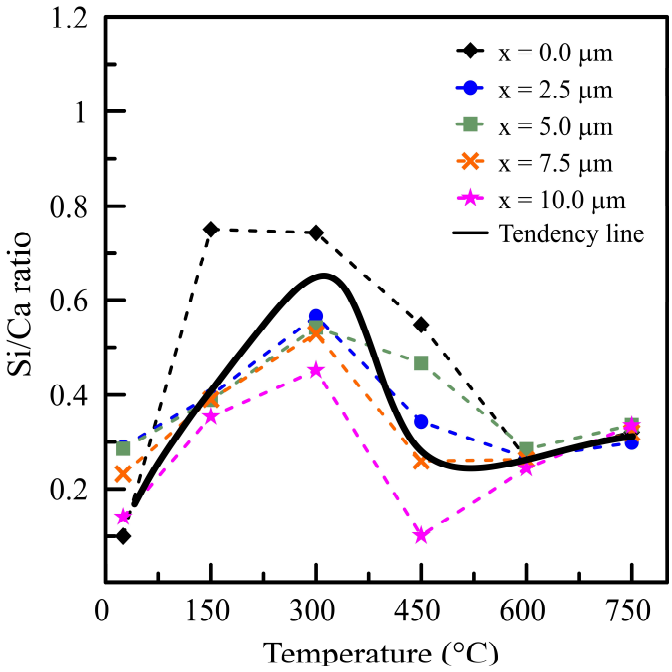

Figure 12 – Si/Ca ratio as a function of temperature and distance from fractured surface

At the temperature range between 150 and 300 °C, the Si/Ca ratio exhibits an increasing tendency. Considering that very limited data is available in the literature regarding the effect of temperature on the Si/Ca ratio of hydrated products, the origin of this behavior cannot be precisely determined based on SEM/EDS results alone. This investigation requires specific studies that aim to investigate the chemical and mineralogical changes in the vicinity of the fiber, which is a methodological challenge given the significantly reduced size of this region. Even though this specific experimental investigation is out of the scope of this paper, a few possible scenarios may be discussed.

356 The first hypothesis is that the thermal energy provided may work as a catalyst for the
357 topochemical reaction of anhydrous silicates (i.e. C_3S and C_2S) that are deposited on the
358 interfacial transition zone. This reaction may occur with silicates that are either partially
359 hydrated or non-hydrated, which have been found in the interfacial transition zone in SEM
360 imagery (see Fig. 11). Additionally, recently published studies pointed out that the temperature
361 range between 100 and 400 °C is favorable for the formation of new hydration products capable
362 of filling the pores of concrete [37,38]. This hypothetical hydration process could lead to the
363 densification of the interfacial transition zone due to the formation of hydrated products and
364 affect the bond-slip behavior of the hooked-end steel fibers.

365 The second hypothesis is based on the fact that the vicinity of the fiber has a considerable
366 amount of portlandite in room temperature conditions (see Fig. 12). In this sense, the increase
367 in temperature acts as a catalyst to the pozzolanic reaction between the $Ca(OH)_2$ rich interfacial
368 transition zone and the SiO_2 present in the concrete mix. Literature results show that the increase
369 in temperature has been responsible for the significant increase in the compressive strength for
370 lime-pozzolan mortars [39,40], which may be another factor that indicates the plausibility of
371 the hypothesis proposed. According to recent studies, the presence of SiO_2 in the ITZ is so
372 significant that the coating of steel and carbon fibers with nano-silica significantly reduced the
373 ITZ porosity around the fiber matrix and improved the interfacial adhesion [41,42].

374 What is particularly concerning about the two hypotheses proposed is that both require water
375 for the chemical reaction to occur. In this sense, the steam generated by the evaporation of free,
376 adsorbed, and interlayer water results in the increase of the internal pressure in the mortar and
377 induces an internal autoclaving condition [43]. Therefore, the water required could be trapped
378 inside the specimen in the form of steam and superheated water, associated with the gas-liquid-
379 solid triple point of a substance. Superheated water occurs between the usual boiling
380 temperature (~100 °C at 1 atm) and the critical temperature of 374 °C in pressured
381 environments. This pressured environment could be provided by the low porosity and limited

382 permeability of the mortar used in this study, which has a compressive strength of ~90 MPa
383 (see Section 3.1).

384 In this context, the fiber-matrix interface is composed of three main phases at room temperature:
385 the steel fiber, an interfacial transition zone (mostly portlandite), and the cementitious matrix.
386 The increase in temperature within the range between 25 and 450 °C leads to changes in the
387 Si/Ca ratio of the interfacial transition zone and the debonding of fibers seems to occur between
388 the steel fiber and the interfacial transition zone. For temperatures equal or higher than 450 °C
389 the oxidation process of steel fibers becomes relevant, which means that a new phase is present
390 in the fiber-matrix interface. Therefore, the fiber-matrix interface can be described as having
391 four phases: the steel fiber, the oxide layered structure, the interfacial transition zone, and the
392 cementitious matrix. This oxide formation leads to an increase in the confinement forces applied
393 in the steel fiber and change the location where the fracture occurs from fiber-matrix to oxide-
394 matrix, which are both factors that affect the bond-slip mechanism.

395 **3.3 Bond-slip behavior**

396 Figure 13 shows both the individual and averaged load-displacement curves obtained
397 experimentally for each target temperature. The maximum pullout load (P_{L1}) accounts for the
398 energy required to yield the hooks at two points, while the lower peak (P_{L2}) is associated with
399 the force required to straighten the fiber. The load values at a displacement of 10 mm (P_{L3}) were
400 used to evaluate the changes in the dynamic frictional interaction between fiber and matrix.
401 Table 5 shows the load values of P_{L1}, P_{L2}, $P_{L3,}$ and the observations made during the pullout
402 tests, as well as the standard deviation values. The results presented show that the temperature
403 exposure tends to increases the dispersion of the experimental curves even in a double-sided
404 pullout test using multiple fibers; however, this dispersion increase is not as significant as in
405 single-fiber pullout tests found in the literature [16].

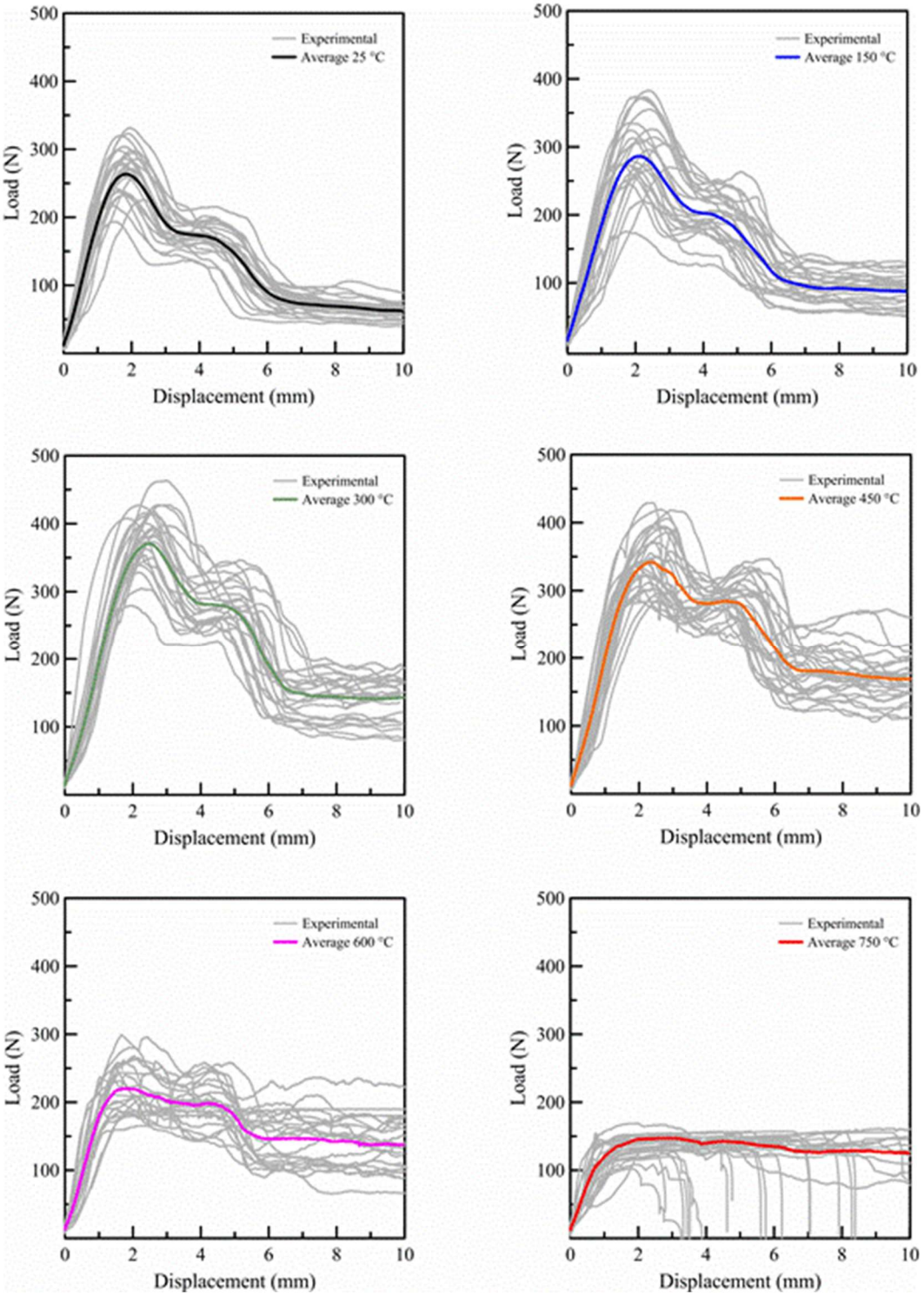

406

407 Figure 13 – Experimental and average load-displacement curves obtained for each target temperature

408

409

410

411

Table 5 – Load values of P_{L1}, P_{L2}, P_{L3} and the observations that were made during the pullout tests

Temperature (°C)	P_{L1} (N)	P_{L2} (N)	P_{L3} (N)	P_{L1}/P_{L2}	Observation
25	269.0 (± 34.9)	177.3 (± 21.0)	61.2 (± 11.3)	1.52	NFR in 30 specimens
150	297.1 (± 50.2)	203.4 (± 33.5)	85.3 (± 22.4)	1.46	NFR in 30 specimens
300	378.3 (± 45.9)	285.4 (± 32.0)	134.5 (± 34.5)	1.33	NFR in 30 specimens
450	350.1 (± 46.1)	295.5 (± 27.3)	157.0 (± 28.7)	1.18	NFR in 30 specimens
600	227.1 (± 36.3)	209.6 (± 34.9)	121.3 (± 42.7)	1.08	3 FR in 03 specimens 2 FR in 04 specimens 1 FR in 08 specimens NFR: 15 specimens
750	140.8 (± 16.1)	139.6 (± 12.9)	114.3 (± 23.9)	1.01	4 FR in 15 specimens 3 FR in 05 specimens 2 FR in 03 specimens NFR: 07 specimens

NFR – no fiber rupture; FR – fiber rupture

For specimens exposed to temperatures of 600 °C, it is possible to observe the occurrence of pullout and rupture of steel fibers (see Table 5). This suggests that for temperatures of 600 °C and above the tensile strength of fibers is exceeded before the shear strength of the fiber-matrix interaction. Considering that the peaks P_{L1} and P_{L2} are directly associated with the yielding of the hooks, the changes in the P_{L1}/P_{L2} ratio can be used as a qualitative indirect method to verify the tendency changes in the mechanical interlocking caused by the fibers. Since elevated

420 temperatures affect the microstructure of the cement paste and the ITZ as a whole, the reduction
421 of the P_{L1}/P_{L2} ratio may be attributed mainly to changes in the properties of steel fibers.

422 Results obtained are presented in Table 5, confirming that the P_{L1}/P_{L2} values significantly
423 reduce as temperature increases. This reduction may be evidence that the bending stiffness of
424 the steel fibers substantially reduces after temperature exposure, and could suggest that the
425 mechanical interlock provided by the hooks is negligible for temperatures of 600 °C and above.
426 This would also confirm that the dynamic frictional interaction between fiber and matrix is the
427 preponderant factor in this temperature range. Furthermore, the reduction in bending stiffness
428 is associated with the effects of elevated temperatures on the physical, mechanical, and
429 microstructural properties of hooked-end steel fibers, mainly due to the oxidation and
430 recrystallization processes. These temperature-related processes have shown to significantly
431 increase the grain-size structure of the fiber for temperatures of 600 °C and above [32].

432 Figure 14 illustrates the effect of temperature on the average load-displacement curves and the
433 maximum values of P_{L1}, P_{L2}, and P_{L3}. The maximum pullout load (P_{L1}) values have shown an
434 increasing trend up to 450 °C. In this sense, the P_{L1} values increased by 10.5%, 40.6%, 30.2%
435 for the respective target temperatures of 150, 300, and 450 °C when compared to room
436 temperature results. This increasing tendency may be associated with the Si/Ca ratio changes
437 that may occur in the interfacial transition zone (see Section 3.2), which may result in increased
438 interfacial chemical adhesion and enhances the dynamic frictional interaction between fiber and
439 matrix due to the densification of the ITZ. Since the bond-slip response is sensitive to normal
440 stresses, the changes in the Poisson's ratio of the materials [5] and the shrinkage behavior of
441 the cementitious matrix up to ~300 °C [29] may influence the results obtained.

442

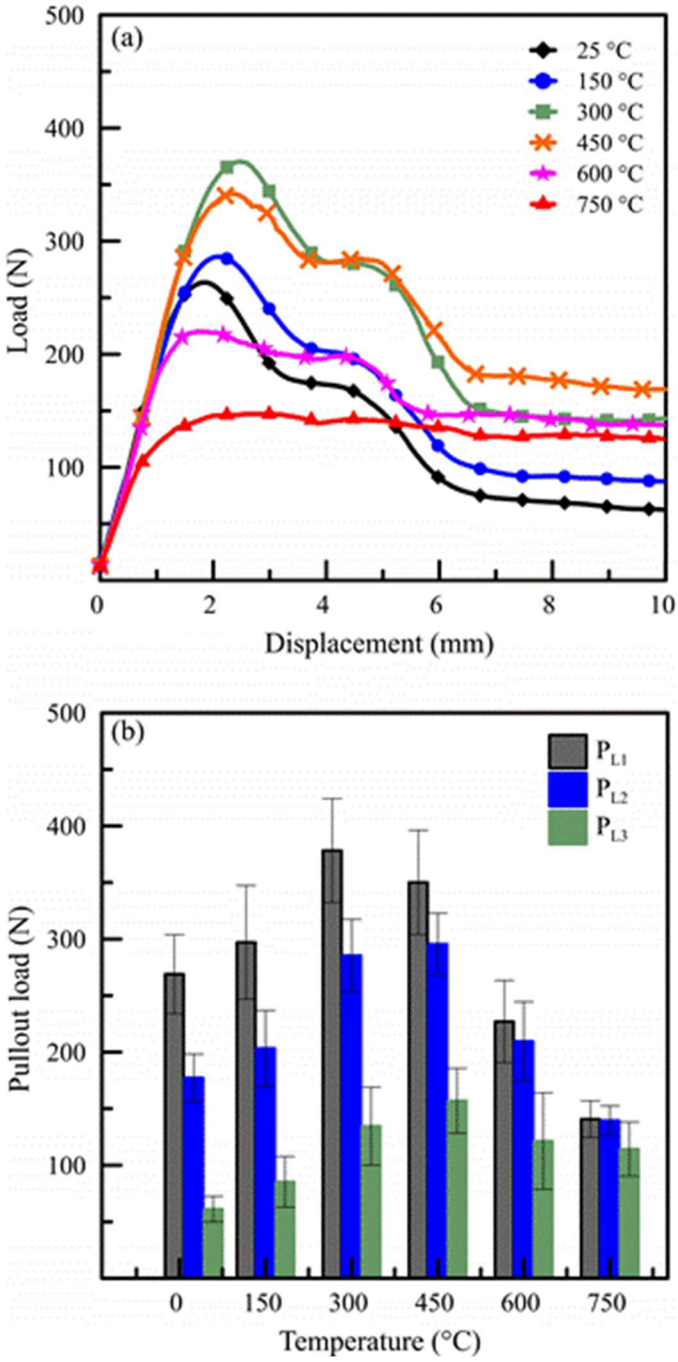

Figure 14 – Effect of temperature on (a) the average load-displacement curves and (b) the maximum values of P_{L1}, P_{L2}, and P_{L3}

Although an increasing trend is verified in this study, literature results show that the values of P_{L1} remain relatively constant up to ~400 °C [13–16]. This negligible effects of temperature on P_{L1} values may be associated with two main factors. The first factor is that literature results were obtained using less stable test methods than the one proposed in this study, which increases the dispersion and may result in the non-significance of results. The second is that the ITZ remains relatively unchanged when compared to the cement paste up to the dehydration

452 temperature of portlandite (~450 °C [44]) since the region in the vicinity of the fiber contains a
453 considerable volume of $CaOH_2$ crystals (see Section 3.2).

454 After exposure to temperatures of 600 and 750 °C, a reduction trend was observed in the P_{L1}
455 values with the respective reductions of 15.6% and 47.6% when compared to room temperature
456 results. This reduction is mainly associated with the drastic reductions in the bending stiffness
457 of steel fibers, as previously determined by the analysis of the P_{L1}/ P_{L2} ratio, and the dehydration
458 of hydrated products in the ITZ. Even with those considerations, additional factors that
459 significantly influence the evidenced behavior can be cited, such as the coarsening of the ITZ
460 pore structure, the significant cracking caused by the thermal gradients, and the reversible
461 transformation of quartz from α-trigonal to β-hexagonal at 573 °C [29].

462 The values of P_{L3} significantly increase by 39.4%, 119.8%, 156.6%, 98.2%, and 86.7% for the
463 respective temperatures of 150, 300, 450, 600, and 750 °C when compared to room temperature
464 results. It is also important to notice that the maximum increase is detected at 450 °C, which
465 may be associated with the changes in the Si/Ca ratio in the interfacial transition zone and the
466 initial oxidation of steel fibers. Even for temperatures of 600 °C and above a significant increase
467 is verified in terms of P_{L3} when compared to room temperature results. This increase may be
468 attributed to the increase in the confining forces and the changes in the fracture mechanism
469 from fiber-matrix to oxide-matrix, discussed in Section 3.2. Another relevant aspect is that the
470 increase in the confining forces may be associated with the shrinkage suffered by the cement
471 paste for temperatures above 300 ºC, which can easily overcome 1.6% [29,45].

472 **3.4 Admissible error and sample size determination**

473 Figure 15 shows the sample size required as a function of the admissible error for the peak load
474 values P_{L1}, P_{L2}, and P_{L3}. The analysis conducted using inferential statistics and a 95%
475 confidence interval shows that the sample size increases with the reduction of the admissible
476 error for the pullout test. This increase in sample size is particularly greater for the P_{L3} values
477 both in room conditions and after exposure to elevated temperatures, which can be justified by

the reduced stability during the dynamic portion of the test and the consequent increase in the variability of results.

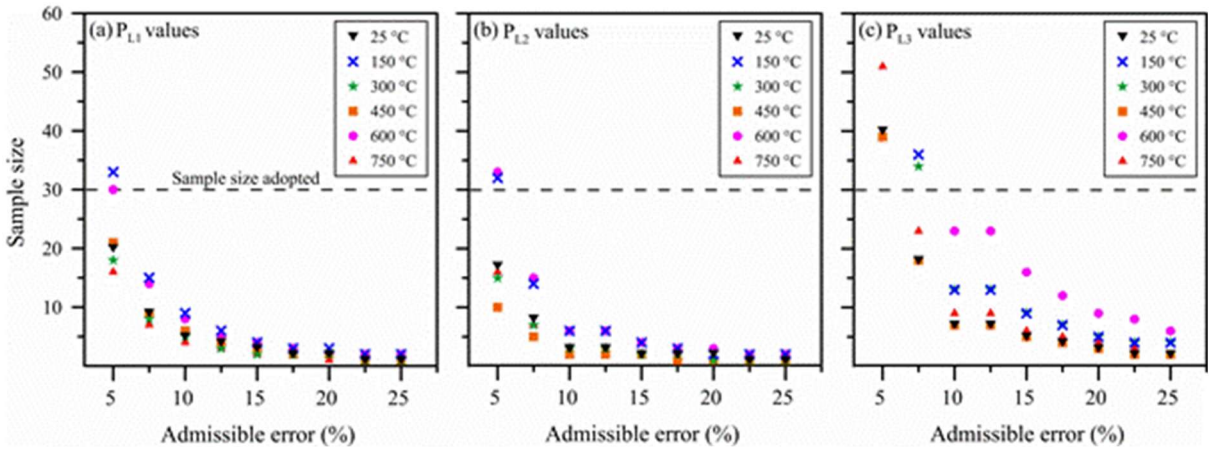

Figure 15 – Sample size required as a function of the admissible error for the (a) P_{L1} values, (b) P_{L2} values, and (c) P_{L3} values

It is possible to observe that the sample size of 30 pullout specimens adopted in this study was enough to ensure an admissible error of ~11%. Moreover, a total of 16 pullout specimens ensure a maximum admissible error of ~15% and 9 pullout specimens a maximum admissible error of ~20% for all the peak loads evaluated. In this sense, the results obtained using double-sided and with multiple fibers have shown an acceptable error for the purpose. This suggests that the adoption of a double-sided pullout test using multiple fibers may be a stable and adequate test method to improve the reliability of the pullout results obtained, both in room conditions and after exposure to elevated temperatures.

Even with those considerations, the results regarding the admissible error of the pullout test proposed in this paper (double-sided, multiple fibers) could not be compared with the tests found in current literature (single-sided, single fiber). The comparison was not possible because the standard deviation values are not provided in studies found in the literature [13–16]. Therefore, the experimental data reported in this work serves as a reference for comparison for future works that aim to study the effect of temperature on the bond-slip of steel fibers.

4. Numerical simulation

In this section, the numerical approach proposed by Bitencourt et al. [18] for modeling steel fiber reinforced concrete (SFRC) is employed. This is one of the most appropriate approaches available in literature for the numerical simulation of pullout tests since the model allows representing the fiber/matrix interaction separately.

Figure 16 illustrates the 3D model constructed for the numerical simulations of the pullout tests. As can be seen in this figure, the fibers are represented discretely and explicitly and a crack is predefined at the central part of the specimen, as considered in the laboratory tests. Therefore, the interaction between the top and bottom parts is given by the fiber/matrix interface. The bottom part of the specimen is fixed, while a vertical displacement of 10 mm with a displacement rate of 0.5 mm/min is imposed at the top part, as depicted in the Figure 16a.

Initially, fibers and mortar matrix are discretized in finite elements in a totally independent way (non-conforming meshes) using two-noded truss finite elements and four-noded tetrahedral finite elements, respectively. Then, five-noded tetrahedral coupling finite elements (CFEs) are inserted (see light blue elements in Figure 16b) to describe the fiber-matrix interaction [46].

In this work, the behavior of the fibers is described by a one-dimensional elastoplastic material model, while the mortar matrix is idealized with a linear elastic behavior. The fiber/matrix interaction is described by the non-rigid version of the CFEs, and a continuum damage model, by adjusting the parameters obtained in the laboratory tests. Details about the fiber/matrix interaction and a comparison with an analytical model can be found in Bitencourt et al. [18].

It is important to mention that the effect of the hooks is distributed along the length of a straight fiber in the numerical model. This simplification has proven to be a feasible manner to represent hooked-end steel fibers in the model since the effect of the hooked-end is considered in the bond-slip law adopted. Recently, this numerical strategy was successfully employed for modeling three-point bending tests (3-PBT) to predict the post-cracking parameters of SFRC [47] and the behavior of beams with combined reinforcement of steel fibers and rebars [48].

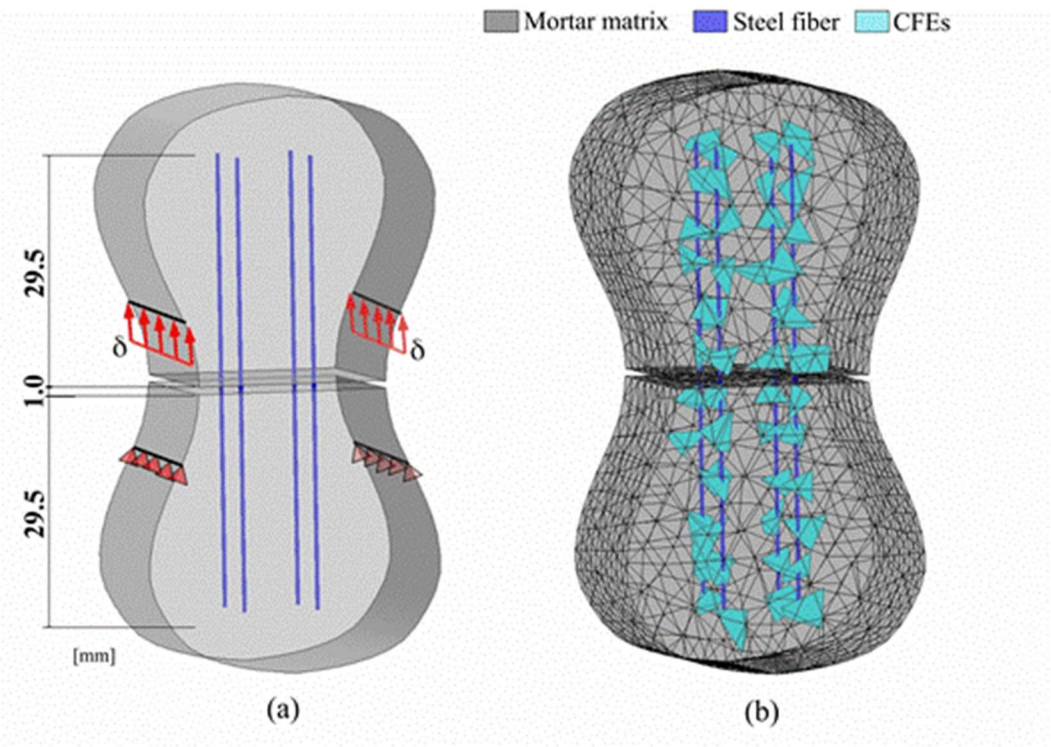

Figure 16 –3D model for the numerical simulation of the pullout tests: (a) geometry of the specimen, boundary conditions and imposed displacement, and (b) discretization in finite elements

In the numerical analyses performed, the mortar matrix was discretized by 8,165 four-noded tetrahedral finite elements, whereas 11 two-noded truss finite elements were used for each steel fiber. To couple the initially independent meshes of the mortar matrix and steel fibers, 48 five-noded tetrahedral CFEs were added.

The behavior of the CFEs, given by a continuum damage model is adjusted to describe the response of the pullout test at room temperature. Therefore, a bond-slip model defined by the relationship between the shear stress (adherence stress) and relative sliding is initially constructed for the temperature of 25° according to the response presented in Fig. 14a. An appropriate damage coefficient is introduced in the constitutive equation based on the experimental responses to capture the responses for other temperatures. In the following sections, the definition of the damage coefficient, and the bond-slip model are presented as the main constitutive parameters for the definition of the fiber-matrix interaction.

4.1 Fiber-matrix interaction

539 **4.1.1 Damage coefficient**

540 In this section, the damage coefficient (K_i) and the factors of change (k_{Ln}) that are applied in
541 the constitutive model as the effect of temperature on the bond-slip behavior of the hooked-end
542 steel fibers are presented. Figure 17 illustrates the analytical model for the damage coefficient
543 as a function of temperature. One damage coefficient (K_i) is generated for each major peak of
544 the bond-slip model, therefore K_1, K_2, and K_3 for the respective peak loads of P_{L1}, P_{L2}, and P_{L3}.

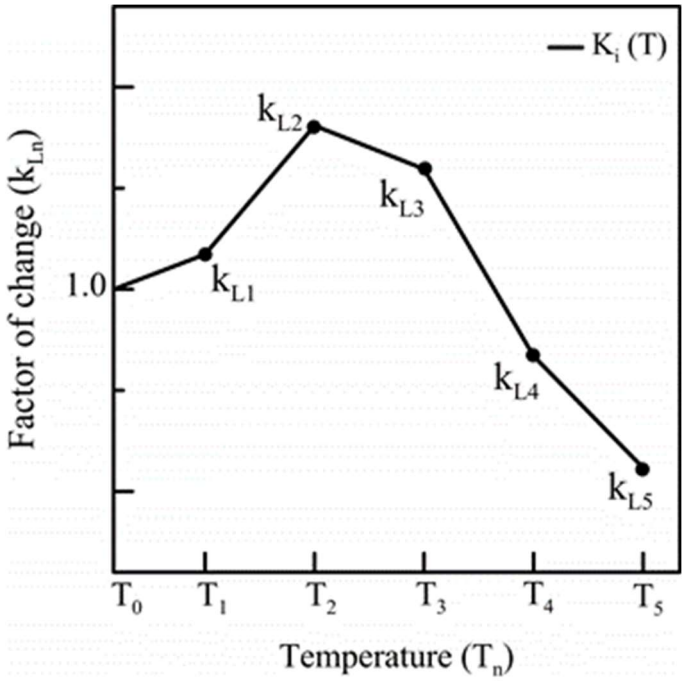

545

546 Figure 17 – The analytical model for the damage coefficient as a function of temperature

547 The factors of change (k_{Ln}) are determined based on the value of one of the peak loads (P_{Li})
548 after exposure to a given temperature (T_n) related to room temperature (T_0) results, which is
549 calculated as:

$$k_{Ln} = \frac{P_{Li}(T_n)}{P_{Li}(T_0)} \qquad \text{Eq. (3)}$$

550 The damage coefficient (K_i) is a multilinear equation that interpolates the factor of change for
551 other temperatures than the temperatures evaluated. Therefore, the analytical equation for K_i
552 can be defined as a function of temperature, as follows:

$$K_i = \begin{cases} 1 + (k_{L1} - 1)\dfrac{(T - T_0)}{(T_1 - T_0)} & if\ T_0 \le T\ \le T_1 \\ k_{L1} + (k_{L2} - k_{L1})\dfrac{(T - T_1)}{(T_2 - T_1)} & if\ T_1 \le T\ \le T_2 \\ \vdots & \\ k_{L(n-1)} + \left(k_{Ln} - k_{L(n-1)}\right)\dfrac{\left(T - T_{(n-1)}\right)}{\left(T_n - T_{(n-1)}\right)} & if\ T_{(n-1)} \le T\ \le T_n \end{cases} \quad \text{Eq. (4)}$$

4.1.2 Bond-slip

A constitutive model for the bond-slip behavior of hooked-end steel fibers after exposure to elevated temperatures is proposed. The shear stresses associated with P_{L1}, P_{L2}, and P_{L3} used as input in the model may be calculated by the simplified assumption that the shear stress is constant, and the effect of the hook is distributed along the length of the fiber, as follows:

$$\tau_{bn} = \frac{P_{Ln}}{\pi * d * l_e} \quad \text{Eq. (5)}$$

where τ_{bn} is the average shear stress for a given peak load; P_{Ln} is the respective load value for P_{L1}, P_{L2}, or P_{L3}; d is the diameter of the steel fiber; l_e is the embedded length of the fiber in the cementitious matrix. In this sense, the bond stresses (τ_b) between the substrate and the hooked-end steel fiber for pullout and splitting failure are given as a function of the slip (s) along the axis of the fiber, as follows:

$$\tau_b(s) = \begin{cases} K_1.\tau_{b1}\left(\dfrac{s}{s_1}\right)^a & if\ 0 \le s\ \le\ s_1 \\ K_1.\tau_{b1} - (K_1.\tau_{b1} - K_2.\tau_{b2})\left(\dfrac{s - s_1}{s_2 - s_1}\right) & if\ s_1 \le s\ \le\ s_2 \\ K_2.\tau_{b2} & if\ s_2 \le s\ \le\ s_3 \\ K_2.\tau_{b2} - (K_2.\tau_{b2} - K_3.\tau_{b3})\left(\dfrac{s - s_3}{s_4 - s_3}\right) & if\ s_3 \le s\ \le\ s_4 \\ K_3.\tau_{b3} & if\ s \ge s_4 \end{cases} \quad \text{Eq. (6)}$$

where K_1, K_2, and K_3 are the analytical equations that relate the factors of change for the peaks of P_{L1}, P_{L2}, and P_{L3}, respectively. The shear stresses τ_{b1}, τ_{b2}, and τ_{b3} account respectively for the shear generated by P_{L1}, P_{L2}, and P_{L3} for the steel fibers at room temperature (see Eq. 5),

566 while the variable s is the slip of fibers in the cementitious matrix. Figure 18 shows the curve
567 defined by the Eq. 6.

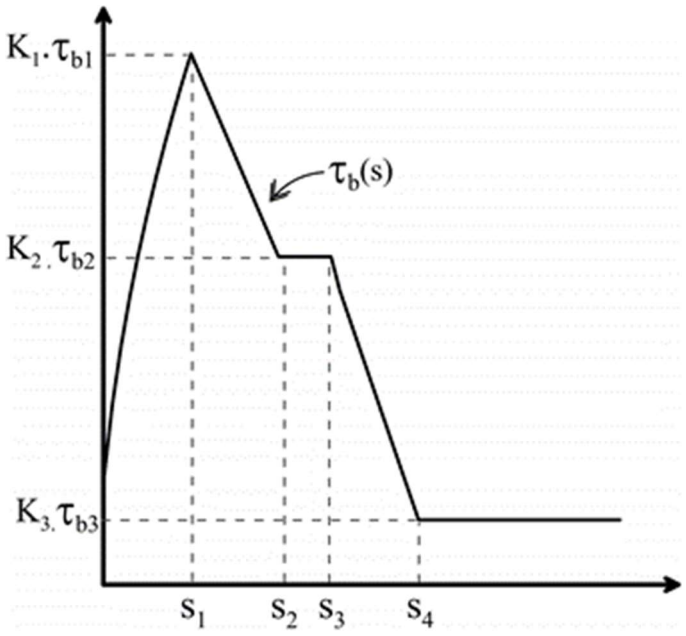

568

569 Figure 18 – Bond-slip constitutive model for the hooked-end steel fibers after elevated temperatures

570 By assuming that the function $q(r)$ represents the hardening/softening law of the continuum
571 damage model assumed to describe the fiber-matrix interaction, the Eq. 6 can be rewritten in
572 terms of these stress (q) and strain (r) like internal variables by considering the relationship
573 $q(r) = \tau_b\left(\frac{r}{k}\right)$, as follows:

$$q(r) = \begin{cases} K_1.\tau_{b1}\left(\dfrac{r/k}{s_1}\right)^a & if\ 0 \le r/k \le s_1 \\ K_1.\tau_{b1} - (K_1.\tau_{b1} - K_2.\tau_{b2})\left(\dfrac{r/k - s_1}{s_2 - s_1}\right) & if\ s_1 \le r/k \le s_2 \\ K_2.\tau_{b2} \quad if\ s_2 \le r/k \le s_3 & \\ K_2.\tau_{b2} - (K_2.\tau_{b2} - K_3.\tau_{b3})\left(\dfrac{r/k - s_3}{s_4 - s_3}\right) & if\ s_3 \le r/k \le s_4 \\ K_3.\tau_{b3} \quad if\ r/k \ge s_4 & \end{cases} \qquad \text{Eq. (7)}$$

574 where k is the coupling parameter in the direction normal to the fiber, varying from 10^6 to 10^9
575 (MPa/mm) according to the recommendation of Bitencourt et al. [46]. More details about the
576 numerical model for SFRC may be found in the work of Bitencourt et al. [18].

577 The mortar matrix is assumed as a linear elastic material with Poisson's ratio of ν = 0.2 and the
578 elastic modulus (E_c) determined based on the experimental characterization conducted for each
579 target temperature. The behavior of the steel fibers is given by an elastic perfectly plastic model,
580 with an elastic modulus of E_f = 210 GPa for all target temperatures, since the initial interatomic
581 distance of the metallic ions is not changed after the steel fibers are exposed to the heat-cooling
582 process [49,50]. The yield stress (σ_y) of the steel fibers as a function of temperature was
583 estimated based on the rate of change obtained in the experimental work conducted by Abdallah
584 et al [13] applied to the tensile strength of the steel fiber used in this study. The damage
585 coefficient values were calculated based on the peak load values (P_{L1}, P_{L2}, and P_{L3}) presented
586 in Table 5 of Section 3.3. Table 6 shows a summary of the parameters adopted in the numerical
587 simulations.

588 Table 6 – Summary of the parameters adopted in the numerical simulations

Target temperature (°C)	Bond-slip parameters											Mortar properties		Steel fiber properties	
	τ_{b1} (MPa)	τ_{b2} (MPa)	τ_{b3} (MPa)	s_1 (mm)	s_2 (mm)	s_3 (mm)	s_4 (mm)	a	K_1	K_2	K_3	f_c (MPa)	E_c (GPa)	σ_y (MPa)	E_f (GPa)
25	3.9	2.6	0.9	0.9	2.3	3.5	5.6	0.7	1.0	1.0	1.0	89.3	40.0	1240	210
150	3.9	2.6	0.9	1.0	2.7	3.5	5.6	0.6	1.1	1.1	1.3	85.5	34.2	1226	210
300	3.9	2.6	0.9	1.2	2.7	3.9	5.7	0.7	1.4	1.6	2.0	72.3	29.4	1199	210
450	3.9	2.6	0.9	1.2	2.7	4.0	5.6	0.6	1.3	1.6	2.3	57.6	23.2	1032	210
600	3.9	2.6	0.9	0.8	2.3	3.5	4.8	0.6	0.8	1.1	2.0	42.3	12.8	463	210
750	3.9	2.6	0.9	0.8	2.3	3.5	4.8	0.6	0.6	0.8	1.7	26.0	9.4	336	210

589

590 **4.2. Numerical results**

591 Figure 19 shows the average experimental curves compared to the numerical simulation
592 conducted in this study. It is confirmed that the numerical curves are capable of describing the
593 bond-slip behavior of fibers as a function of temperature. In this sense, a good agreement
594 between the experimental and numerical results is observed.

595 The value adopted for the slip parameter s_1 in the numerical simulation is the half of that
596 obtained in the experimental results. Moreover, the other slip parameters (i.e. s_2, s_3, and s_4) are
597 defined as the experimental slip value subtracted by the half of the slip parameter s_1. The
598 difference in terms of slip values can be explained by the slip mechanism that occurs in double-
599 sided pullout specimens.

600 For slip values up to the peak load P_{L1}, both sides of the pullout specimen are experiencing the
601 mechanical anchorage of the hooks and fiber slipping. In general lines, half of the total slip can
602 be attributed to each side of the pullout specimen. Once the hook is straightened in one of the
603 sides, the slip mechanism is similar to the single-sided pullout tests. Therefore, the difference
604 between experimental and numerical values of slip occurs since the Eq. 5 was developed
605 considering the pullout test of a single fiber embedded on one side, while the fibers are
606 embedded on both sides in the pullout tests performed in this research. This difference in terms
607 of slip values was also reported by other researchers in the literature. According to Lee et al.
608 [51], the slip s_1 for fiber embedded on both sides is about twice that obtained with fiber
609 embedded on one side and this difference between responses decreases as smaller is the fiber
610 embedded length.

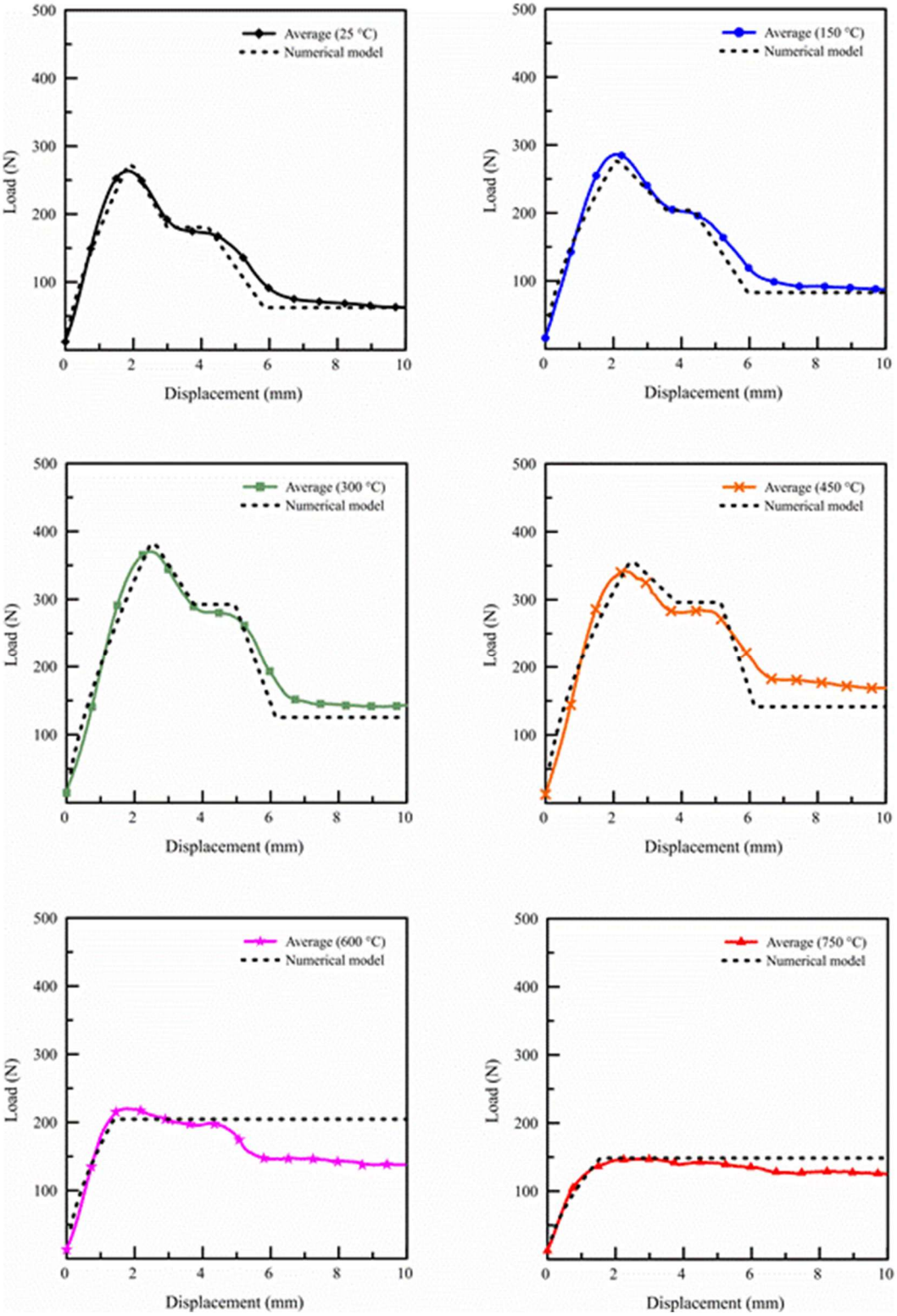

Figure 19 – Average experimental load curves compared to the numerical simulation

Figure 20 shows the fiber stress at the crack compared to the tensile strength of steel fibers, and the stress distribution for temperatures of 25 and 750 °C. Comparing the results, it can be observed that in the temperature range of 25 and 450 °C the governing mechanism can be attributed to the shear interaction between the steel fibers and the cementitious matrix since the

tensile stresses generated on the steel fibers are not sufficient to cause fiber rupture. For specimens exposed to temperatures of 600 and 750 °C, the tensile strength of the steel fibers is reached, therefore fiber rupture occurs. This can also be noticed in the numerical simulations in Fig. 19. Additionally, the difference between the experimental and numerical results for T = 600 °C may be attributed to the fact that the numerical model does not account for partial yielding of the steel fibers as occurred for the experimental results (see Table 5, column "Observations"), and instead considers that all steel fibers reach the yield strength at the same time.

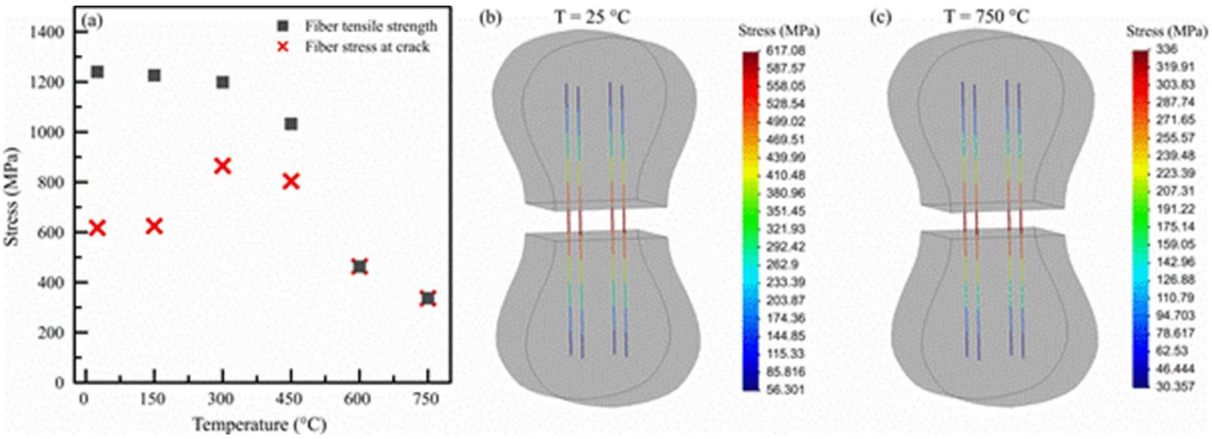

Figure 20 – Effect of temperature on (a) the fiber stress at the crack, and the stress distribution for (b) T = 25 °C and (c) T = 750 °C

This suggests that for temperatures of 600 °C and above the tensile strength of fibers is exceeded before the shear strength of the fiber-matrix interaction (see Fig. 20a). This behavior is in line with the experimental results presented in Table 5 and Figure 14 of this study. The significant reduction of the tensile strength of steel fibers can be attributed to the reduction of grain boundary surface due to the grain-growth process induced by temperature [32]. In summary, the governing mechanism changes from bond-slip behavior to the tensile strength capacity of fibers for temperatures of 600 °C and above.

5 Conclusions

The following conclusions can be drawn from the present study:

- The compressive strength and elastic properties of the mortar reduced linearly with temperature increase. The compressive strength was reduced by 4.2% (150 °C) to 70.9% (750 °C) and the dynamic elastic modulus was reduced by 14.9% (150 °C) to 76.5% (750 °C), both related to room temperature results. These changes were attributed to the severe dehydration of hydrated products and were comparable with the results found in the literature.
- The iron oxide began to form ~450 °C and expanded into the ITZ porosity for temperatures of 600 °C and above. This process resulted in changes in the rupture pattern and the debonding of fibers, which occurred in the interface between the oxide and the matrix. Additionally, the Si/Ca ratio in the region surrounding the steel fibers increased considerably up to 300 °C, denoting changes in the mineralogical properties in the vicinity of the fiber.
- The maximum pullout load values increased up to ~30% in the range of 150 °C ≤ T ≤ 450 °C and decreased up to ~48% for 600 °C ≤ T ≤ 750 °C. Additionally, the dynamic frictional interaction between fiber and matrix increases for all temperatures evaluated. These changes were attributed to the changes in the Si/Ca ratio in the vicinity of the fiber, the oxide formation, and the increase in the confining forces applied to the fibers. Additionally, the bending stiffness of the steel fibers reduced with the increase in temperature and reached a negligible contribution at ~600 °C.
- The numerical model can describe the bond-slip behavior of fibers as a function of temperature with a good agreement between the experimental and numerical results. For 25 °C ≤ T ≤ 450 °C, the governing mechanism is the shear interaction between the fibers and the cementitious matrix. For T ≥ 600 °C, the tensile strength of steel fibers is achieved before the bond-slip can take place. The aforementioned governing mechanisms were confirmed by experimental results and the numerical simulation conducted.

Finally, it must be highlighted that the experimental campaign conducted, and the numerical model developed in this study may serve as a reference for the simulation of mesoscale tests and assessing the behavior of structural elements built with steel fiber reinforced concrete under high temperatures.

Acknowledgments

The authors would like to thank the Institute for Technological Research (IPT) and its foundation (FIPT) for their financial and institutional support through the New Talents Program N.01/2017. The authors would also like to thank the researchers Ph.D. Renata Monte (USP), MSc Priscila Rodrigues Melo Leal (IPT), and Eng. Tiago Haddad Marum (USP) for the technical contributions that improved the quality of this work.

Data availability: The raw/processed data required to reproduce these findings cannot be shared at this time as the data also forms part of an ongoing study. The raw/processed data may be provided by the corresponding author upon request.

References

[1] M. di Prisco, G. Plizzari, L. Vandewalle, Fibre reinforced concrete: New design perspectives, Mater. Struct. 42 (2009) 1261–1281.

[2] R.P. Manfredi, F. de Andrade Silva, Test Methods for the Characterization of Polypropylene Fiber Reinforced Concrete: A Comparative Analysis, KSCE J. Civ. Eng. 24 (2020) 856–866. doi:10.1007/s12205-020-0741-7.

[3] B. Luccioni, G. Ruano, F. Isla, R. Zerbino, G. Giaccio, A simple approach to model SFRC, Constr. Build. Mater. (2012). doi:10.1016/j.conbuildmat.2012.07.027.

[4] N. Banthia, Fiber Reinforced Concrete, ACI SP-142ACI, Detroit, MI. (1994). doi:10.4188/transjtmsj1965a.24.P621.

[5] A. Bentur, S. Mindess, Fibre reinforced cementitious composites, 2nd ed., Taylor & Francis, New York, 2007.

688 [6] S. Abdallah, M. Fan, D.W.A. Rees, Bonding Mechanisms and Strength of Steel Fiber–
689 Reinforced Cementitious Composites: Overview, J. Mater. Civ. Eng. (2018).
690 doi:10.1061/(asce)mt.1943-5533.0002154.

691 [7] F.L. de Oliveira, Design-oriented constitutive model for steel fiber reinforced concrete,
692 Universitat Politècnica de Catalunya, 2010.

693 [8] Victor M. C. F. Cunha, Steel fibre reinforced self-compacting concrete (from
694 micromechanics to composite behavior), 2010. http://hdl.handle.net/1822/10667.

695 [9] Y.W. Chan, S.H. Chu, Effect of silica fume on steel fiber bond characteristics in
696 reactive powder concrete, Cem. Concr. Res. (2004).
697 doi:10.1016/j.cemconres.2003.12.023.

698 [10] F. Laranjeira, C. Molins, A. Aguado, Predicting the pullout response of inclined
699 hooked steel fibers, Cem. Concr. Res. (2010). doi:10.1016/j.cemconres.2010.05.005.

700 [11] Y. Lee, S.T. Kang, J.K. Kim, Pullout behavior of inclined steel fiber in an ultra-high
701 strength cementitious matrix, Constr. Build. Mater. (2010).
702 doi:10.1016/j.conbuildmat.2010.03.009.

703 [12] M.J. Shannag, R. Brincker, W. Hansen, Pullout behavior of steel fibers from cement-
704 based composites, Cem. Concr. Res. (1997). doi:10.1016/S0008-8846(97)00061-6.

705 [13] S. Abdallah, M. Fan, K.A. Cashell, Bond-slip behaviour of steel fibres in concrete after
706 exposure to elevated temperatures, Constr. Build. Mater. 140 (2017) 542–551.
707 doi:10.1016/j.conbuildmat.2017.02.148.

708 [14] S. Abdallah, M. Fan, D.W.A. Rees, Effect of elevated temperature on pull-out
709 behaviour of 4DH/5DH hooked end steel fibres, Compos. Struct. 165 (2017) 180–191.
710 doi:https://doi.org/10.1016/j.compstruct.2017.01.005.

711 [15] S. Abdallah, M. Fan, K.A. Cashell, Pull-out behaviour of straight and hooked-end steel
712 fibres under elevated temperatures, Cem. Concr. Res. 95 (2017) 132–140.
713 doi:10.1016/j.cemconres.2017.02.010.

714 [16] G. Ruano, F. Isla, B. Luccioni, R. Zerbino, G. Giaccio, Steel fibers pull-out after
715 exposure to high temperatures and its contribution to the residual mechanical behavior
716 of high strength concrete, Constr. Build. Mater. (2018).

717 doi:10.1016/j.conbuildmat.2017.12.129.

718 [17] A. Caggiano, E. Martinelli, A unified formulation for simulating the bond behaviour of
719 fibres in cementitious materials, Mater. Des. 42 (2012) 204–213.
720 doi:10.1016/j.matdes.2012.05.003.

721 [18] L. A. G. Bitencourt, O.L. Manzoli, T.N. Bittencourt, F.J. Vecchio, Numerical modeling
722 of steel fiber reinforced concrete with a discrete and explicit representation of steel
723 fibers, Int. J. Solids Struct. 159 (2019) 171–190. doi:10.1016/j.ijsolstr.2018.09.028.

724 [19] R. Serafini, S.R.A. Dantas, R.P. Salvador, R.R. Agra, D.A.S. Rambo, A.F. Berto, A.D.
725 de Figueiredo, Influence of fire on temperature gradient and physical-mechanical
726 properties of macro-synthetic fiber reinforced concrete for tunnel linings, Constr.
727 Build. Mater. 214 (2019) 254–268. doi:10.1016/j.conbuildmat.2019.04.133.

728 [20] S.R.A. Dantas, R. Serafini, R.C. de O. Romano, F. Vittorino, K. Loh, Influence of
729 polypropylene microfibers (PPMF) dispersion procedure on fresh and hardened
730 rendering mortar properties, Ambient. Construído. 20 (2020) 7–23. doi:10.1590/s1678-
731 86212020000200384.

732 [21] J.M. Carpio, R. Serafini, D. Rambo, A. de la Fuente, A.D. De Figueiredo, Assessment
733 of the bearing capacity reduction of FRC elements subjected to fire, in: Proc. Fib
734 Symp. 2019 Concr. - Innov. Mater. Des. Struct., Kraków, Poland, 2019: pp. 1378–
735 1386.

736 [22] U. Schneider, Concrete at high temperatures - A general review, Fire Saf. J. (1988).
737 doi:10.1016/0379-7112(88)90033-1.

738 [23] T. Materne, F. de Buyl, G.L. Witucki, Organosilane Technology in Coating
739 Applications : Review and Perspectives, Dow Corning. (2012).
740 doi:10.1017/CBO9781107415324.004.

741 [24] Federation Internationale du Beton, Model Code for Concrete Structures 2010, in:
742 Ernst & Sohn, Germany, 2013: p. 434.

743 [25] C.M. Judd, G.H. McClelland, C.S. Ryan, Data Analysis : A Model Comparison
744 Approach to Regression, ANOVA, and Beyond, 2009.

745 [26] W. de O. Bussab, P.A. Morettin, Estatística básica, Saraivauni, São Paulo, 2017.

[27] V. Vydra, F. Vodák, O. Kapičková, Š. Hošková, Effect of temperature on porosity of concrete for nuclear-safety structures, Cem. Concr. Res. 31 (2001) 1023–1026. doi:10.1016/S0008-8846(01)00516-6.

[28] E. Gallucci, X. Zhang, K.L. Scrivener, Effect of temperature on the microstructure of calcium silicate hydrate (C-S-H), Cem. Concr. Res. 53 (2013) 185–195. doi:10.1016/j.cemconres.2013.06.008.

[29] Z.P. Bažant, M.F. Kaplan, Concrete at high temperatures: material properties and mathematical models, Longman, 1996.

[30] M.S. Cülfik, T. Özturan, Effect of elevated temperatures on the residual mechanical properties of high-performance mortar, Cem. Concr. Res. (2002). doi:10.1016/S0008-8846(02)00709-3.

[31] E. Horszczaruk, P. Sikora, K. Cendrowski, E. Mijowska, The effect of elevated temperature on the properties of cement mortars containing nanosilica and heavyweight aggregates, Constr. Build. Mater. (2017). doi:10.1016/j.conbuildmat.2017.02.003.

[32] R. Serafini, R.R. Agra, R. Monte, A.D. Figueiredo, The effect of elevated temperatures on the tensile properties of steel fiber reinforced concrete by means of double edge wedge splitting (DEWS) test: Preliminary results, in: G. Pijaudier-Cabo, P. Grassl, C. La Borderie (Eds.), Proc. 10th Int. Conf. Fract. Mech. Concr. Concr. Struct., IA-FraMCoS, Bayonne, France, 2019: p. 6. doi:10.21012/FC10.240385.

[33] R. Serafini, L.M. Mendes, R.P. Salvador, A.D. de Figueiredo, The effect of elevated temperatures on the properties of cold-drawn steel fibers, Mag. Concr. Res. (2020) 1–28. doi:10.1680/jmacr.19.00498.

[34] L.M.S. Mendes, R. Serafini, A.D. de Figueiredo, The effect of high temperature on the mechanical properties of steel fibers and polymeric macrofibers, in: Proc. 9th Int. Conf. Concr. Under Sev. Cond. - Environ. Load., Menvia, Porto Alegre, Brazil, 2019. doi:10.31808/5ca6e03b5ca4f0d406ac888a.

[35] R.P. Salvador, S.H.P. Cavalaro, I. Segura, A.D. Figueiredo, J. Pérez, Early age hydration of cement pastes with alkaline and alkali-free accelerators for sprayed concrete, Constr. Build. Mater. 111 (2016) 386–398. doi:10.1016/j.conbuildmat.2016.02.101.

776 [36] A. Nonat, The structure and stoichiometry of C-S-H, Cem. Concr. Res. (2004).
777 doi:10.1016/j.cemconres.2004.04.035.

778 [37] K.Y. Kim, T.S. Yun, K.P. Park, Evaluation of pore structures and cracking in cement
779 paste exposed to elevated temperatures by X-ray computed tomography, Cem. Concr.
780 Res. (2013). doi:10.1016/j.cemconres.2013.03.020.

781 [38] M.C.R. Farage, J. Sercombe, C. Gallé, Rehydration and microstructure of cement paste
782 after heating at temperatures up to 300 °C, Cem. Concr. Res. (2003).
783 doi:10.1016/S0008-8846(03)00005-X.

784 [39] V. Pachta, S. Triantafyllaki, M. Stefanidou, Performance of lime-based mortars at
785 elevated temperatures, Constr. Build. Mater. 189 (2018) 576–584.
786 doi:10.1016/j.conbuildmat.2018.09.027.

787 [40] R.K. Ibrahim, R. Hamid, M.R. Taha, Fire resistance of high-volume fly ash mortars
788 with nanosilica addition, Constr. Build. Mater. 36 (2012) 779–786.
789 doi:10.1016/j.conbuildmat.2012.05.028.

790 [41] Z. Pi, H. Xiao, J. Du, M. Liu, H. Li, Interfacial microstructure and bond strength of
791 nano-SiO2-coated steel fibers in cement matrix, Cem. Concr. Compos. 103 (2019) 1–
792 10. doi:10.1016/j.cemconcomp.2019.04.025.

793 [42] M. Lu, H. Xiao, M. Liu, X. Li, H. Li, L. Sun, Improved interfacial strength of SiO2
794 coated carbon fiber in cement matrix, Cem. Concr. Compos. 91 (2018) 21–28.
795 doi:10.1016/j.cemconcomp.2018.04.007.

796 [43] H. El-Didamony, E.A. El-Rahman, R.M. Osman, Fire resistance of fired clay bricks-fly
797 ash composite cement pastes, Ceram. Int. (2012). doi:10.1016/j.ceramint.2011.06.050.

798 [44] H.F.W. Taylor, Cement chemistry. 2nd ed., Acad. Press. (1997). doi:10.1016/S0958-
799 9465(98)00023-7.

800 [45] C.R. Cruz, M. Gillen, Thermal expansion of Portland cement paste, mortar and
801 concrete at high temperatures, Fire Mater. 4 (1980) 66–70.
802 doi:10.1002/fam.810040203.

803 [46] L.A.G. Bitencourt, O.L. Manzoli, P.G.C. Prazeres, E.A. Rodrigues, T.N. Bittencourt, A
804 coupling technique for non-matching finite element meshes, Comput. Methods Appl.

805 Mech. Eng. 290 (2015) 19–44. doi:10.1016/j.cma.2015.02.025.

806 [47] Y.T. Trindade, L.A.G. Bitencourt Jr., R. Monte, A.D. de Figueiredo, O.L. Manzoli,
807 Design of SFRC members aided by a multiscale model: Part I – Predicting the post-
808 cracking parameters, Compos. Struct. 241 (2020) 112078.
809 doi:10.1016/j.compstruct.2020.112078.

810 [48] Y.T. Trindade, L.A.G. Bitencourt Jr., O.L. Manzoli, Design of SFRC members aided
811 by a multiscale model: Part II – Predicting the behavior of RC-SFRC beams, Compos.
812 Struct. 241 (2020) 112079. doi:10.1016/j.compstruct.2020.112079.

813 [49] S. James, W. Alexander, Materials Science and Engineering Handbook, 2001.
814 doi:10.1126/science.232.4757.1485.

815 [50] W. Callister, D. Rethwisch, Materials science and engineering: an introduction, 7th ed.,
816 John Wiley, New York, USA, 2007.

817 [51] S.C. Lee, J.Y. Cho, F.J. Vecchio, Diverse embedment model for steel fiber-reinforced
818 concrete in tension: Model development, ACI Mater. J. (2011).
819 doi:10.14359/51683262.

820